Spring 5-3-2022

EFFICIENT ENERGY HARVESTING WITH APPLICATIONS IN VIBRATION AND IMPLANTABLE BIOSENSORS

Mohammad Atmeh
University of Texas at Tyler

Recommended Citation

Atmeh, Mohammad, "EFFICIENT ENERGY HARVESTING WITH APPLICATIONS IN VIBRATION AND IMPLANTABLE BIOSENSORS" (2022). *Mechanical Engineering Theses.* Paper 19.
http://hdl.handle.net/10950/3987

EFFICIENT ENERGY HARVESTING WITH APPLICATIONS IN VIBRATION AND IMPLANTABLE BIOSENSORS

by

MOHAMMAD ATMEH

A thesis submitted in partial fulfillment of the
requirements for the degree of
Master of Science in Mechanical Engineering
Department of Mechanical Engineering

Alwathiqbellah Ibrahim, Ph.D., Committee Chair

College of Engineering

The University of Texas at Tyler
April 2022

The University of Texas at Tyler
Tyler, Texas

This is to certify that the Master's Thesis of

MOHAMMAD ATMEH

has been approved for the thesis requirement on

14 April 2022

For the Masters of Science in Mechanical Engineering

Approvals:

DocuSigned by:
Alwathiqbellah Ibrahim
3A3F3DF38EA844C...
Thesis Chair: Alwathiqbellah Ibrahim, Ph.D.

DocuSigned by:
Nael Barakat
30D27AF79E60404...
Member: Neal Barakat, Ph.D.

DocuSigned by:
Tahsin Khajah
ACA7690059AD419...
Member: Tahsin Khajah, Ph.D.

DocuSigned by:
Nael Barakat
30D27AF79E60404...
Chair, Department of Mechanical Engineering

DocuSigned by:
Javier A. Kypuros
3E50E32BE8F046A...
Dean, College of Engineering

Acknowledgments

All praise is duo to God, who blessed my career with success. I would like to express my deepest appreciation and gratitude to my supervisor and committee chair, Dr. Alwathiqbellah Ibrahim for the continuous support. He continually conveyed a spirit of adventure and challenge, assistance and teaching. Without his care and guidance, nothing of this thesis would be possible.

It is a great pleasure to thank my committee members, Dr. Nael Barakat and Dr. Tahsin Khajah, who supported and guided me with their insightful knowledge throughout my career. Also, my deepest gratitude goes to my mother and father for their everlasting care and support, prayers, and continuous encouragement. I am thankful also to Dr. Yahia Al-Smadi for his support and guidance.

In addition, I would like to thank my fellow labmates, Mostafa, Qais, Hadeel, and Katy for the stimulating research environment and all the enjoyment we had. Finally, I am genuinely appreciative to my friends, Hesham, Hamad, Nedal, Mahmoud, and Mohammad for their valuable advises, assistance, and time to push my career forward.

Table of Contents

Appendices

List of Tables

List of Figures

Abstract

The world has stepped into the fourth industrial revolution in many ways such as using the internet of things (IoT) in various applications, and removing the rechargeable power sources seeking for batteryless systems. Since energy is widely abundant around us and it is going to waste, numerous of recent studies have been conducted to propose sustainable solutions to harvest the free ambient power from the surrounding and convert it into electricity. Heat energy, kinetic energy, and radio waves are examples of these potentially harvestable energy sources. Mechanical vibrations represent one of the most plentiful forms of kinetic energy that can be scavenged by different techniques, such as electromagnetic and piezoelectric energy harvesters. As an application, utilizing the human body to harvest energy for wireless autonomous medical applications is under investigation. Therefore, developing safe, efficient, and biologically-compatible energy harvesters to be implanted inside the human body motion is critical to the success of such applications. Triboelectric generators to be installed inside the knee implant in the Total Knee Replacement (TKR) and the hip implant in Total Hip Replacement (THR) for self-powered load monitoring have been proposed.

Duo to the inability of traditional scavenging techniques to generate enough energy from low-frequency ambient vibrations, a frequency up-converter vibration energy harvester is proposed. The harvester converts low-frequency vibrations to high-frequency self-oscillation through a mechanical frequency up-converter using a magnetic coupling, thus providing more efficient energy conversion at low frequencies. The harvester consists of two cantilever beams with tip magnets facing each other at the same polarity. The low-frequency beam is made of polymer, while the high-frequency beam is made of Aluminum. The high-frequency beam is a bimorph fully covered with piezoelectric layers. A lumped parameter of the two degrees of freedom model (2DOF) is utilized to simulate the dynamic behavior and the generated voltage signal. The static response of the resonators shows a threshold distance of $15mm$ between the two magnets where the system has monostable oscillations above the threshold and bistable oscillations below the threshold. Furthermore, the dynamic behavior of the resonators is investigated at monostable, threshold, and bistable regions for different excitation levels. The harvester's output voltage at different resistance values is extracted from the model. The frequency up-converter was found to effectively scavenge energy from low-frequency external vibrations by mechanically up-converting the ambient vibrations to high-frequency self-oscillations.

Validating the proposed frequency up-converter experimentally has been done with modifying

some of the simulation parameters such as the physical dimensions and converting the high-frequency beam (HFB) into a unimorph fully covered with a single piezoelectric layer. The static analysis of the system reveals a threshold distance of $15mm$ that divides the system into a monostable regime for weak magnetic coupling and a bistable regime for strong magnetic coupling. Hardening and softening behaviors were observed at the low-frequency range for the mono and bistable regimes, respectively. In addition, a combined nonlinear behavior of softening and hardening behaviors was captured for low frequencies at the threshold distance. Furthermore, the proposed system generates voltage showing 100% increment at the threshold compared to the monostable regime. Lowering the separation distance to reach the bistable range, $d \leq 8mm$, will increase the generated voltage compared to the voltage generated in the monostable and threshold. The simulated and experimental results were in good agreement. Moreover, the effect of changing the external resistance was investigated, and setting the external resistance to $25M\Omega$ was found to maximize the generated voltage.

To satisfy biomedical implants continuous need for improvement; triboelectric energy harvesters continue to show promising and efficient performance in transferring mechanical energy into electrical energy, making them a prime candidate for biomedical implants. TKR is a widely used surgery worldwide and, more so, in the United States. Therefore, Triboelectric harvester performance in biomedical applications was investigated in TKR. In this study, performance

of two new configurations a triboelectric energy harvester in TKR were compared as self-powered implanted sensors for load measurement. The first configuration is a full knee harvester, covering the whole area of the tibial tray. The second configuration consists of two harvesters at the lateral and medial locations. Both configurations are to be fit in the knee implant. Performance of both configurations experimentally was evaluated while subjected to an axial cyclic load applied by a dynamic tester at different frequencies. Also, the lateral and medial generators were tested for load imbalance detection producing promising results. Findings from this study would contribute to the improvement of TKRs by transforming them from passive to smart TKRs using the proposed energy harvesters, which will lead to better health monitoring.

Similarly, Total Hip Replacement (THR) involves a conventional medical implant where many interacting factors could cause patient dissatisfaction, sometimes leading to lengthy and risky procedures based on guesses. Energy harvesting from natural human motion is being investigated to create a reliable source that will power smart implants and monitor performance simultaneously without any replacement or exchanges. A novel Triboelectric Energy Harvester (TEH) design was proposed to retrofit a TEH to the THR implant, making it a smart implant. A custom femoral head was designed to incorporate grooves onto the THR femoral head, maximizing energy production without increasing the overall size of them.

The TEH consists of two Titanium layers separated by a polydimethylsiloxane (PDMS) insulator. The Finite Element Analysis shows that the mechanical spring maintains the contact separation motion which is the working cycle of the of the TEH for voltage generation. A theoretical model of a single-degree-of-freedom system with piece-wise functions was proposed based on the FEA results to model the contact and release modes and voltage estimations. This study can open the door and lead to new research in load monitoring for total hip replacement.

Chapter One

Introduction

The continuous development in technology has recently led to improve power generation resources by transferring them from conventional to non-conventional. Conventional power resources such as batteries are limited due to their short lifespan and the limited ability to store the power, so they need charging every time. Therefore, harvesting energy from the ambient becomes an attractive concept to remove the need for batteries due to their limitations. [6]. Mechanical vibrations are considered one of the most forms of mechanical energy wasted that is abundant around us in the environment, in addition to our daily living activities, such as the motion of the vehicles and human motions. [7–9]. Consequently, research is constantly conducted to utilize those mechanical vibrations to generate electricity from mechanical vibrations to power wireless sensors and electronics that work in micro-to-milliwatts range [10].

Nature is rich with the mechanical vibrations that are abundant at low-frequency ranges [11].

So, harvesting those vibrations utilizes the ambient energy to engage the non-conventional power resources[12]. Different mechanisms are used to convert the mechanical vibrations into electrical power, where electromagnetic [13], triboelectric [14, 15], and piezoelectric [16] energy harvesters are the most common. Among all these mechanisms, piezoelectric energy harvesters have the ability to work at a low-power level and resist environmental conditions, therefore, they have been utilized in several applications, such as being implanted inside the human body [17, 18], civil infrastructure [1, 19], and the aerospace systems [20–24]. However, some drawbacks of the harvesters include the high resonance frequency which is away from the ambient ranges [7, 25], and the narrow bandwidth [26]. Therefore, several techniques have been utilized to overcome these drawbacks, such as the nonlinearity contribution [27–34], circuit management [35], double pendulum system [36], frequency-tunable oscillators [37–39], and frequency up-conversion [2]. Nonlinearity has been utilized to expand the bandwidth of the output power through influencing the mechanical [40, 41], impact [42], and magnetic [34, 43, 44] effects.

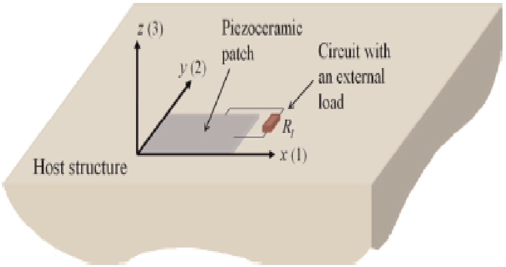

Figure 1.1. Example of proposed piezoceramic patch attached onto a large civil engineering structure for power generation.[1]

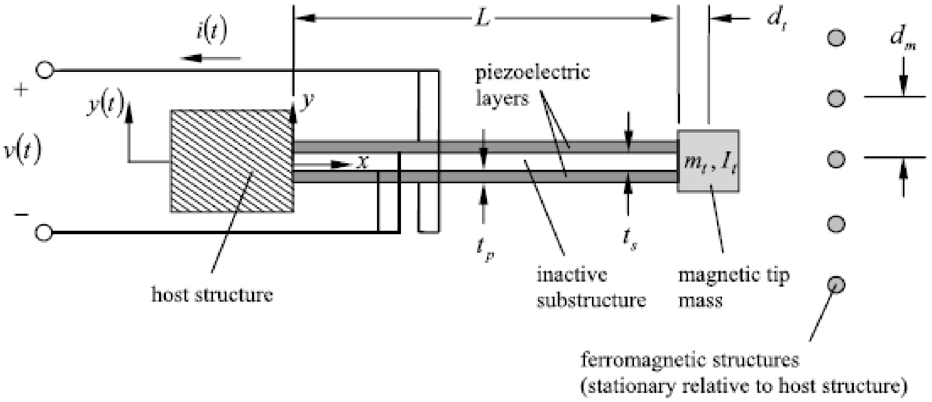

Figure 1.2. Example of proposed Layout and geometric parameters of cantilevered vibration energy harvester in parallel bimorph configuration with magnetic tip mass (Frequency Up-conversion)[2].

To increase the efficiency of harvesting energy at low frequency vibrations, the frequency up-converter has been investigated lately [2, 45–53]. The idea of the frequency up-converter is that the low-frequency sources can induce high-frequency oscillations [54]. This induction can be obtained either by the impact [55] or pluck [56]. An impact between low-frequency beam and the high-frequency beam will transfer the low-frequency vibrations into high-range frequencies [45,57]. This technique would improve the low-frequency vibration harvesters by filling the gap between the low-frequency excitation, and high-frequency response [58,59]. To increase the reliability and eliminate issues of mechanical contact, the possibility of using a magnetic coupling has been investigated and optimized as a non-mechanical contact method [2,3,48,60,61]. The low-frequency motions of animals have been up-converted through a self-powered magnetoacoustic into high-frequency acoustic signals [62]. On the other hand, in a different study, an electromagnetic frequency up-converter induction was used with magnets and coils at the top of the resonator beam to generate power [61].

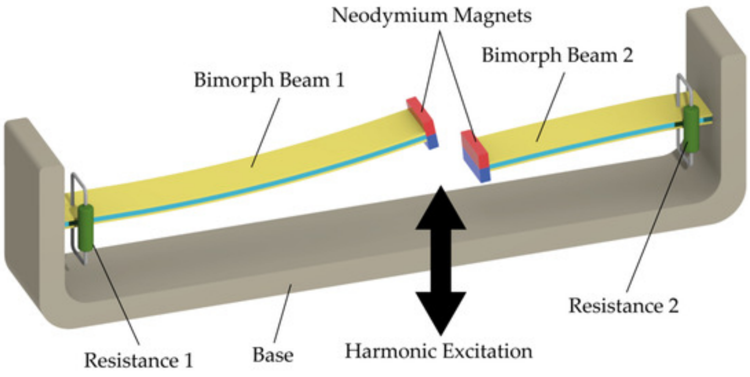

Figure 1.3. Example of proposed Optimized Magnetically Coupled Two-Degree-of-Freedom Bistable Energy Harvester.[3]

The nonlinear magnetic behaviors of softening and hardening hwere the natural frequency of the resonators can be achieved by controlling the separation distance between two magnets facing each other at the same polarity [34]. Broadening the bandwidth has been investigated by using microscale [63–65] or macroscale [25] monostable energy harvesters. Also, bistability was used to increase the frequency bandwidth, and the magnitude of the output power [26, 66]. Other studies used the same method for improving the output energy [67–72]. Experimental results show that maximum power is produced at the transition region between the monostable and the bistable regions [34, 73, 74]. Also, it was shown that the external load resistance was optimized in a magnetically coupled two degree of freedom bistable energy harvester to maximize the output power [3]. The effect of spring stiffness at low excitation frequencies under the Gaussian white noise excitation at a low excitation level has a significant impact on improving the harvesting efficiency in bistable energy harvesters [75].

In biomedical applications, the satisfaction level of TKR surgery is influenced by ongoing issues stemming from implant resilience, function loosening, and load imbalance, among other factors. These factors are usually associated with the magnitude of the loads transferred to the joint; thus, the possibly of noninvasively monitoring these loads would significantly improve surgical intervention decisions. A battery-powered system is sometimes fitted with the joint to power the load sensors intraoperatively (for sensor-aided soft tissue balancing). Still, these are usually removed from the joint after surgery [76]. Therefore, having energy harvesting mechanisms working independently with wireless networks presents a viable option to eliminate the use of batteries [7].

A telemetered TKR system was developed to function postoperatively for sensing and monitoring the joint loads[76–78]. Sensors capable of self-powering through harvesting energy from joint loads provide a long-term functionality in TKR to monitor the loads continuously[4, 79–82]. Piezoelectric sensors are the most widespread in biomechanical applications as they fulfill self-powering and sensing requirements [4, 83–86]. However, their biocompatibility and cost are still disadvantageous when compared to triboelectric-based harvesters and sensors.

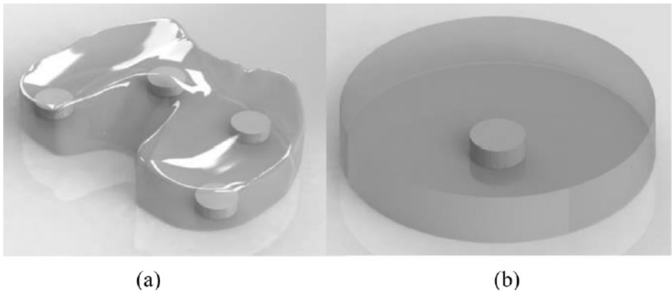

Figure 1.4. Example of proposed embedded piezoelectric sensor in the polyethylene bearing in TKR.[4]

The triboelectric effect is characterized by transferring electrons inductively from one material to another when they come in and out of contact. It occurs due to the affinity difference to gain or lose electrons [87, 88]. Due to its advantages such as biocompatibility, high efficiency, low fabrication costs, and lightweight, the triboelectric generator has been used recently in wide range of energy harvesting applications [89, 90]. The feasibility of the triboelectric energy harvester in powering electronic circuitry for load sensing has been tested and reported in the literature with relatively high efficiency [91]. The triboelectric harvester generates a voltage signal dependent on the harvester's design parameters. These parameters include the gap size between the mating parts, the thickness of the harvester's material, and external resistance, to name a few. These parameters have been designed and configured to fit the harvester in a TKR to monitor the knee loads[5]. Estimating the knee loads by the triboelectric generator can help determine the wear in polyethylene, stress distribution in the implant and the implant-bone interface, and the stress transferred to the underlying bone[92].

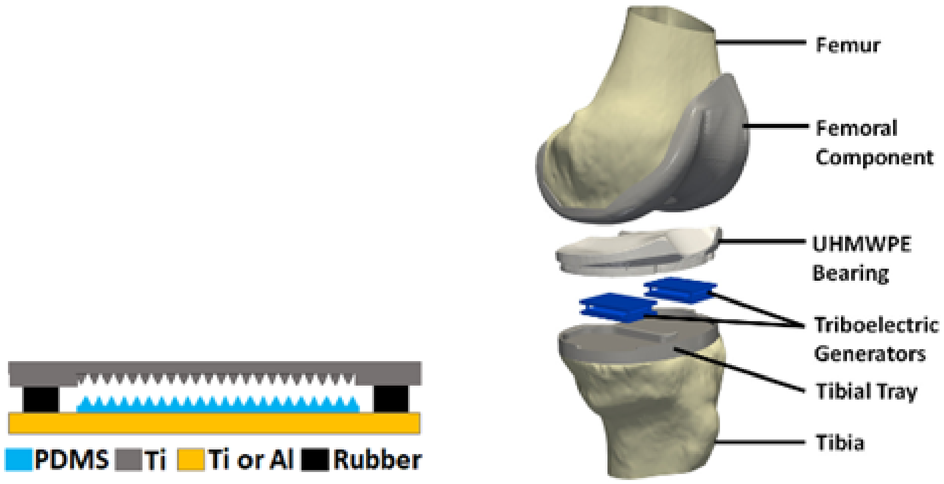

Figure 1.5. Example of proposed performance of a triboelectric transducer when subjected to simulated gait loading[5].

Implantable sensors can increase patient care and medical procedure satisfaction rates by allowing noninvasive diagnostics to be performed to monitor healing or understand unseen conditions within the body [93]. Total Hip Replacement (THR) is considered one of the most common orthopedic surgeries, which are performed over 370,000 times in the United States [94]. Patient dissatisfaction is not easily predictable and does not always have a clear cause; however, a contributing cause of patient dissatisfaction is persisting pain after total hip replacement [95].

In previous years, predominately senior patients have received orthopedic implants; however, the number of younger patients (less than 60 years old) continues to rise due to injuries or being over-weight [96]. Because of this, it is essential to consider implant lifespan and fatigue. The magnitude of loads exerted on the hip joint varies, depending on body weight and joints' kinematics under daily living activities. Forces of approximately eight times the body weight (BW) are usually exerted on is the hip joint [97]. Unpredictable forces acting on the hip lead to common problems associated with THR, such as loosening of prostheses, implant wear, and hence shortening of implant survival rates [98].

Understanding and estimating these forces via smart implants would allow significant improvement in extending the lifespan of implants and consequently increasing overall patient satisfaction [99]. The data provided from smart implants can assist in defining load conditions for testing and verification of implant performance in vitro [100]. Post-operation information regarding the complicated loads acting on the implants could greatly enhance projections about functionality and lifespan. Conventional implants do not provide information regarding the experienced loads; therefore, necessary implant intervention may be recognized at a later stage, showing implant damage in asymptomatic patient. Introducing a smart hip implant that can noninvasively and accurately measure the loads acting on the implants in real-time would provide a multitude of benefits, including diagnostic capabilities [101–103], cost reduction [102], and development of next-generation implants and surgical mechanisms [104, 105].

Energy harvesting and sensing have previously been implemented in human knees because of their relatively simpler geometry. One method of harvesting energy is using piezoelectric implant technology. A piezoelectric material can be placed in the total knee replacement to measure the compressive loads acting on the knee [4]. Triboelectric energy harvesting is another method that is based on power generation caused by contact and separation of materials with opposite tendencies to lose or gain electrons [87, 88]. The greater amount of surface area materials shares, the greater charge can be produced [91]. A point of significance regarding this technology is that the TEH's voltage is proportional to the load acting on the sensor; therefore, a TEH can simultaneously be used as a load sensor and power source.

The contact initiates electrification and electrostatic induction, which generates electricity. Triboelectric energy harvesters are preferred because of their high efficiency, lightweight, and low fabrication costs [91]. Under applied dynamic pressure, charges are generated from the two contact surfaces' friction in the triboelectric generation, which is ideal for a joint such as the hip. However, implementing the triboelectric energy harvesting mechanism in the THR presents a significant challenge due to the complicated nature of the hip joint shape and motion.

Chapter Two

Overview of the Thesis

This chapter aims to give an overview of the topics discussed in this thesis. The problem statement, methodology, and the contribution of each topic of this thesis were highlighted.

Frequency Up-Converter

Problem Statement

The main research motivation for vibration based-energy harvesting is to power small electronic devices using ambient vibration energy to reduce or eliminate the maintenance cost of battery replacement. Among different transduction mechanisms, piezoelectric is considered one of the most efficient techniques for transferring vibrations into useful energy because of the large power density and ease of use. However, several ambient vibrations are at very low frequencies, and designing a piezoelectric energy harvester that would resonate at such low frequencies would require impractically large dimensions and/or big proof masses. Toward this, a frequency up-converter of two magnetically coupled Cantilever beams has been introduced.

Methodology

A piezoelectric energy harvester of two magnetically coupled cantilever beams was subjected to different base excitation levels using an electrodynamics Shaker. One of the beams is fabricated from a soft polymer material with low natural frequency and named a Low-Frequency Beam (LFB), while the second beam is made of Aluminum with high natural frequency and is called a High-Frequency Beam (HFB). For a frequency-up conversion, a piezoelectric strip fully covers the top face of the HFB, while the LFB is kept free of piezoelectric materials. The harvester dynamics have been investigated under different repulsive magnetic forces by controlling the distance between the two magnets. A lumped parameter modeling of a 2DOF system is used to simulate the dynamics of the harvester and its ability to act as a frequency-up converter. Also, a Vibration Controller from Vibration Research Inc was used for getting the experimental results. The shooting method was used in solving the system numerically.

Contribution

As reported in the literature, the frequency up-converter has been investigated previously with different structures and mechanisms. The design of two magnetically coupled cantilever beams was investigated as energy harvester targeting low-frequency ranges. However, the novelty of the work comes from modifying the design by making one of the cantilevers beams a high-frequency beam (above the ambient frequencies) range and with an attachment of a piezoelectric layer while leaving the other cantilever beam at a low-frequency range (below the ambient frequencies) to achieve a unique design for frequency up-converter system, which to the best of our knowledge, never have been investigated before. This study utilized magnetic nonlinearity to transfer the energy between the low and high-frequency ranges. Moreover, inducing the magnetic nonlinearity shows great potential for harvesting more energy and overcoming the narrow bandwidth drawbacks of the linear harvesters. Furthermore, mathematically, the system using a lumped parameter modeling for predicting the harvester's behavior at the monostable, threshold, and bistable regimes for different excitation levels has been modeled. The mathematically simulated results have been validated experimentally. Finally, a combination behavior of softening and hardening nonlinear behaviors at the transition between monostable and bistable regions has been caught, which never have been reported in the literature for this structure.

Total Knee Replacement (TKR)

Problem Statement

TKR was investigated by many studies in the energy harvesting field to create self-powered mechanisms to be integrated with the implant to improve its performance and increase its lifetime. Piezoelectric materials, wireless transmitters, and triboelectric generators were investigated to generate power from the knee under the daily life activities cycles. However, the natural imbalance that is presented inside the knee between the lateral and medial locations was not explored despite it is one of the main causes of the function loosening of the knee implant.

Methodology

A full knee configuration of Triboelectric generator that covers the entire knee area has been investigated under cycling load to study the generated voltage under different amounts of loads and frequencies. Also, the full configuration of the triboelectric generator was divided into two identical generators installed at the lateral and medial locations inside the knee to detect the imbalance. Lastly, a comparison of the generated voltage between the full knee configuration and the lateral and medial configurations was discussed.

Contribution

It has been found that applying higher loads and frequencies on the generator leads to generate higher voltage in both configurations duo to higher generated electrical charges in the triboelectric generators. Also, duo to higher area of contact in the full configuration, the amount of the produced voltage is higher in the full configuration than the combined voltage of both lateral and medial generators as the proportionality of the results shows. Moreover, since both the lateral and medial generators are identical, the generated voltage was approximately equal for both when the load is applied at the center of the knee between both generators. To detect the imbalance inside the knee, the applied load was shifted towards the medial generator. Consequently, it has shown the that generated voltage magnitude was higher in the medial generator than the lateral generator. This result pledge to help in determining the force distribution inside the knee which will contribute to the improvement of the implant while it is manufactured and postoperatively with no need for a power source.

Total Hip Replacement (THR)

Problem Statement

Similar importance to the knee, the Total Hip Replacement (THR) has become recently a hot topic to be explored and developed. Scientists and engineers in energy harvesting have studied the possibility of creating a self-powered sensor to be embedded in the hip for measuring the load distribution by measuring generated power. Strain gauges, pressure sensors, and in vivo studies were conducted to explore the implant force distributions. A novel design is presented in this study by installing the triboelectric generator in the hip to estimate the generated loads inside the joint by measuring the generated voltage at different loads and loading frequencies.

Methodology

A new structure of the hip implant was fabricated from the triboelectric generator. The accetabular cup was replaced by the lower electrode of the triboelectric generator as hemisphere for design fitting. The femoral head of the THR was changed to be the upper electrode of the generator with taking the characteristics of the femoral head design with making grooves along the surface for higher generated voltage. The PDMS in the generator works at the mean time as a plastic spacer, which is a part of the hip implant. The three main components were attached to each other by identical pins that work as springs for maintaining contact and separation. The design was investigated at different loads to determine the optimum linear displacement that will determine the maximum thickness of the PDMS which will provide the optimum applied load. The spring constant of the identical pins was calculated using Hooke's law ($k = F/x$) to know the required stiffness that maintains the contact and separation properly.

Contribution

It is the first study that uses the triboelectric generator in THR as a self-powered mechanism for load monitoring. Also, the triboelectric generator copied the characteristics of the actual THR design with retrofitting the generator and the actual function of the implant motion. Besides, FEA and piecewise functions were utilized to predict the generated voltage as a function of the applied load within the range of contact and separation modes.

Chapter Three

Piezoelectric Energy Harvester Using Frequency Up-Conversion

Modeling and Simulation Analysis

In this section, a piezoelectric vibration energy harvester using frequency up-conversion for energy scavenging from low-frequency external vibrations has been proposed. A mechanical frequency up-converter of two magnetically coupled cantilever beams was used to covert low-frequency vibrations to high-frequency oscillations. The two cantilever beams with tip magnets facing each other at the same polarity were used to induce coupling and nonlinearity for more efficient energy production. A two-degree of freedom-lumped parameter model was presented and the dynamic behavior was simulated to generate voltage signal. First, the analysis started by demonstrating the device configuration and the operation mechanism of the frequency up-converter energy harvester. Then, a theoretical coupled two degree of freedom lumped parameter model has been developed. Additionally, the static response problems has been extracted. Finally, the results have been discussed.

Device Configuration and Operation

The nonlinear frequency up-converter consists of two cantilever beams with tip masses attached to a rigid holder (Fig. 3.1a). The beam to the left in Fig. 3.1a is made of a polymer material to have low natural frequency, and it is called Low-Frequency Beam (LFB), while the beam to the right is a bimorph beam made of Aluminum to increase its natural frequency, and fully covered by piezoelectric laminates for voltage generation, and it is called High-Frequency Beam (HFB). The tip masses are two identical magnets facing each other at the same polarity to create a nonlinear repulsive force that acts as a mechanical coupling between both beams. In Fig. 3.1a, L_1 and L_2 are the lengths of the LFB and HFB, respectively, while R and d are the resistance connected to the piezoelectric strip and the horizontal separation distance, respectively. The mechanical coupler will transfer the energy of the HFB to the range of the LFB to create a frequency up-converter energy harvester. The entire system is subjected to a harmonic base excitation, $a(t)$. By lowering the separation distance between the two magnets, the repulsive force between the two magnets increases and induces high nonlinearity in the system. With high nonlinearity, the potential energy of the resonator will transfer from a monostable system (oscillation of the resonator around the horizontal axis) to a bi-stable system (oscillation of the resonator either upper or lower the horizontal axis). This interaction between the two beams as a function of the separation distance is illustrated in Figure 3.1b. Increasing the distance between the two magnets results in a monostable system where each beam will oscillate around a single well stable equilibrium potential energy function, case 1 in Fig. 3.1b. On the other hand, decreasing the distance between the two magnets will force the system to become bistable, and each beam oscillates between two potential wells around two stable equilibrium points, cases 2 and 3 in Fig. 3.1b.

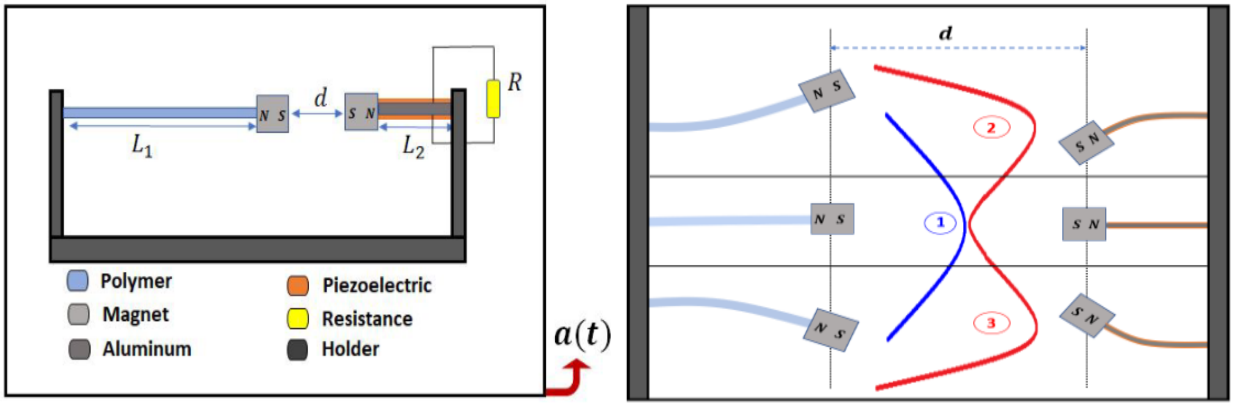

(a) **(b)**

Figure 3.1. Proposed frequency up-converter energy harvester: (a) Device configuration, (b) Device operation.

Theoretical Model

The frequency up-converter will vibrate under mechanical excitation, providing the bending and stress required for piezoelectric voltage generation, Fig. 3.2a. The two magnets will affect each other with the same magnitude of magnetic force but in the opposite direction that can be analyzed into horizontal and vertical components. Here, the frequency up-converter is modeled as a two Degree of Freedom (2DOF) lumped parameter model subjected to harmonic base excitation as shown in Fig. 3.2. For obtaining the electrical equation, the piezoelectric layer is replaced with a capacitance (C_P), and a current source denoted with $I(t)$. An effective electrical circuit is needed for all electrical connections to present a unified formulation for the electrical equation. Fig. 3.3a shows the bimorph in series connection. The equivalent capacitance and resistive load for the effective electrical circuit are shown in Fig. 3.3b. Accordingly, the governing equations for the frequency up-converter system are given by Eq. (3.10), representing the governing equations for the LFB, HFB, and the electrical coupling equation for the piezoelectric layer with the HFB.

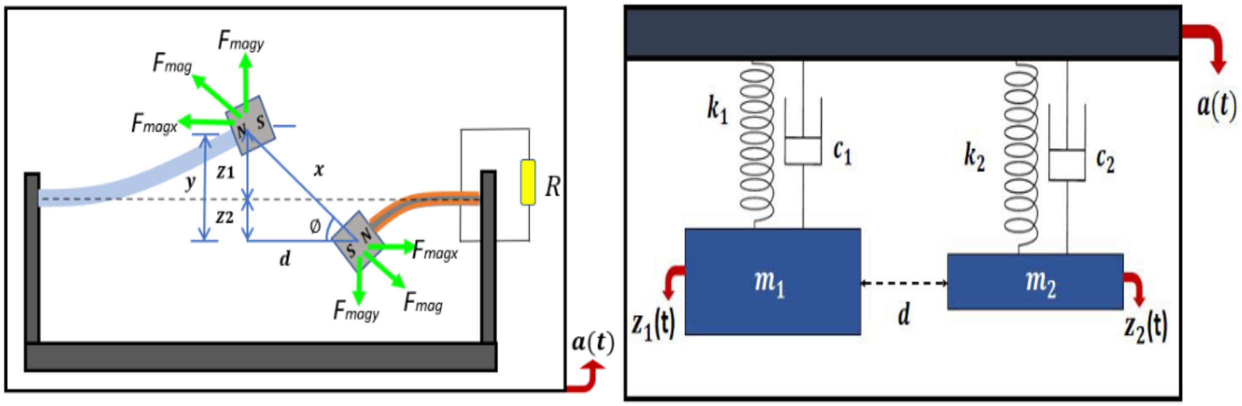

(a) **(b)**

Figure 3.2. (a) Magnetic interactions between LFB and HFB, (b) Two degrees of freedom spring-mass-damper systems for the LFB and HFB.

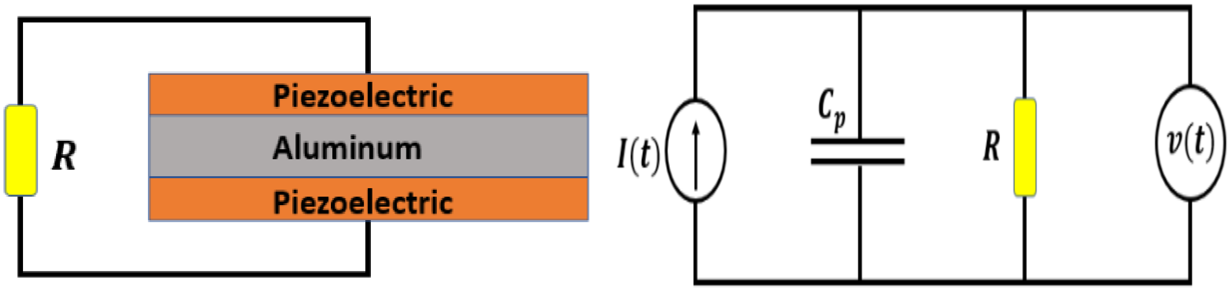

(a) (b)

Figure 3.3. Piezoelectric energy harvester with the equivalent circuit: (a) bimorph in series connection, and (b) the effective circuit for the harvester.

$$
a(t) = \begin{cases} \ddot{z}_1(t) + 2\zeta_1\omega_1\dot{z}_1(t) + \omega_1^2 z_1(t) + \frac{1}{m_1}F_{magy} \\ \ddot{z}_2(t) + 2\zeta_2\omega_2\dot{z}_2(t) + \omega_2^2 z_2(t) + \frac{\theta}{m_2}v(t) - \frac{1}{m_2}F_{magy} \end{cases}. \qquad (3.1)
$$
$$
\dot{v}(t) = \chi\dot{z}_2(t) - \lambda v(t)
$$

Where $a(t)$ is the harmonic base excitation which equals $a(t) = A\ cos(\Omega\ t)$, where Ω is the excitation frequency and A is the amplitude. $z_1(t)$ and $z_2(t)$ are the responses of the LFB and the HFB, respectively. m_1 is the equivalent mass of the LFB, ω_1 is the natural frequency of the LFB, while m_2 and ω_2 are the equivalent mass and natural frequency of the HFB. ζ_1 and ζ_2 denote the damping ratio for the LFB and HFB, respectively. $v(t)$ is the generated voltage from the piezoelectric layers, and $\lambda = 1/RC_p$, such that R is the resistance, and C_p is the capacitance ($C_p = \frac{\epsilon_{33} b_p L_p}{h_p}$), where ϵ_{33} is the permittivity ($3250 \times 8.854 \times 10^{-12}$), b_p, L_p, and h_p are the piezoelectric layer's width, length, and thickness, respectively. Also, χ can be calculated as $\chi = \frac{\theta}{C_p}$, where θ is the coupling coefficient of the piezoelectric layer. The natural frequency of both beams can be calculated from the following formula:

$$f_i = \frac{1}{2\pi}\sqrt{\frac{k_i}{m_i}}\ ,\ i = 1, 2. \tag{3.2}$$

Where k_i is the stiffness of the beams, and can be calculated for the LFB and HFB as: $k_1 = 3E_1I_1/L_1^3$, $k_2 = 3(2E_pI_p + E_2I_2)/L_2^3$, respectively, [106]. E_p and I_p are the modulus of elasticity and moment of inertia of the piezoelectric layer, respectively. m_i is the equivalent mass for each beam. The stiffness of the HFB represents an equivalent stiffness that combines two piezoelectric layers in addition to the beam. Also, the HFB's mass consists of the two piezoelectric layers masses ($2m_p$) and the effective mass of the cantilever beam ($m_{heff} = 0.375m_b$) [106], where m_b is the beam mass.

Magnetic force is the coupling element that transfers the oscillation from the LFB to the HFB. The effect of the distance between the two tip magnets of both beams and the potential energy of the system is illustrated in Fig. 3.1b. Since the magnetic force is a function of the separation distance (d) between the two tip magnets, it will be responsible for producing equilibrium positions of both beams, creating monostable or bistable systems. The total magnetic force between two dipoles is a function of spatial derivatives of their magnetic field and is given by [34]:

$$F_{mag} = \frac{F_R}{X^4} \tag{3.3}$$

Where X is the distance between the centers of the two magnets ($X = \sqrt{d^2 + y^2}$), and F_R is the magnitude of the moments for magnetic dipoles and is given by ($F_R = \frac{3\epsilon q_1 q_2}{2\pi}$), where q_1 and q_2 are the moments of magnetic dipoles for the tip magnets. ϵ is the permeability of the free space and equal to $4\pi \times 10^{-7}\ mkg/s^2A^2$. As shown in Fig. 3.2a, the total magnetic force can be analyzed using the angle ϕ into a horizontal component (F_{magx}), which is assumed to be equivalent to the longitudinal stiffness of the beam, and a vertical component (F_{magy}) in the transverse direction, which is responsible for the beams transverse deflections and is given by the following equation:

$$F_{magy} = \frac{F_R y}{(d^2 + y^2)^{5/2}} \tag{3.4}$$

Where d is the horizontal separation distance between the two magnets, and y is the total deflection between the two moving magnets and given by ($y = z_1(t) + z_2(t)$).

Results And Discussion

Static Analysis

The static analysis of both beams can be formulated by setting all-time derivatives to zero in Eq. (3.1), which leads to the following static equations:

$$k_1 z_{1s} + \frac{F_R(z_{1s} + z_{2s})}{((z_{1s} + z_{2s})^2 + d^2)^{5/2}} = 0 \tag{3.5}$$

$$k_2 z_{2s} - \frac{F_R(z_{1s} + z_{2s})}{((z_{1s} + z_{2s})^2 + d^2)^{5/2}} = 0 \tag{3.6}$$

Where z_{1s} and z_{2s} are the static deflection of the LFB and HFB, respectively. The variables and geometrical parameters needed to solve the system under harmonic excitation are listed in Table 3.1.

The variation of the static deflection for the LFB and HFB's tip magnets centers with varying the distance between them are shown in Figure 3.4, with maximum deflections of $12.6mm$ for the LFB and $0.1mm$ for the HFB. Both static responses show a threshold separation distance d_{th} of $15mm$ that divide the static responses into monostable region ($d > d_{th}$) and bistable region ($d < d_{th}$). Each static response contains a single stable branch for the monostable regime, while it has two stable (upper and lower) branches and one unstable branch (middle) for the bistable regime. The effect of the weight of each tip mass is shown as a symmetry-breaking bifurcation phenomenon at the threshold value.

Table 3.1. Physical and geometrical parameters to be used in the model.

Parameters	**Symbol**	**Value**
LFB (length $\times$*width* $\times$ *thickness*)	$L_1 \times b_1 \times h_1$	$(40 \times 10 \times 1)$ mm
LFB Young's modulus	E_1	2.344 Gpa
LFB Density	ρ_1	1220 kg/m^3
LFB Damping ratio	ζ_1	0.084 N.s/m
HFB (length $\times$*width* $\times$ *thickness*)	$L_2 \times b_2 \times h_2$	$(40 \times 10 \times 1.6)$ mm
HFB Young's modulus	E_2	69.0 Gpa
HFB Density	ρ_2	2700 kg/m^3
HFB Damping ratio	ζ_2	0.0073 N.s/m
Piezoelectric (length $\times$*width* $\times$ *thickness*)	$L_p \times b_p \times h_p$	$(40 \times 7 \times 0.02)$ mm
Piezoelectric Young's modulus	E_p	2450 Mpa
Piezoelectric Density	ρ_p	1780 kg/m^3
Resistance	R	10 MΩ
Magnets side length	L_m	8.0 mm
Magnetic moment	$q_1 = q_2$	0.5 A$^2/m$
Electro-mechanical coupling	θ	1×10^{-4}
Piezoelectric Laminate permittivity	ϵ_{33}	$3250 \times 8.854 \times 10^{-12}$

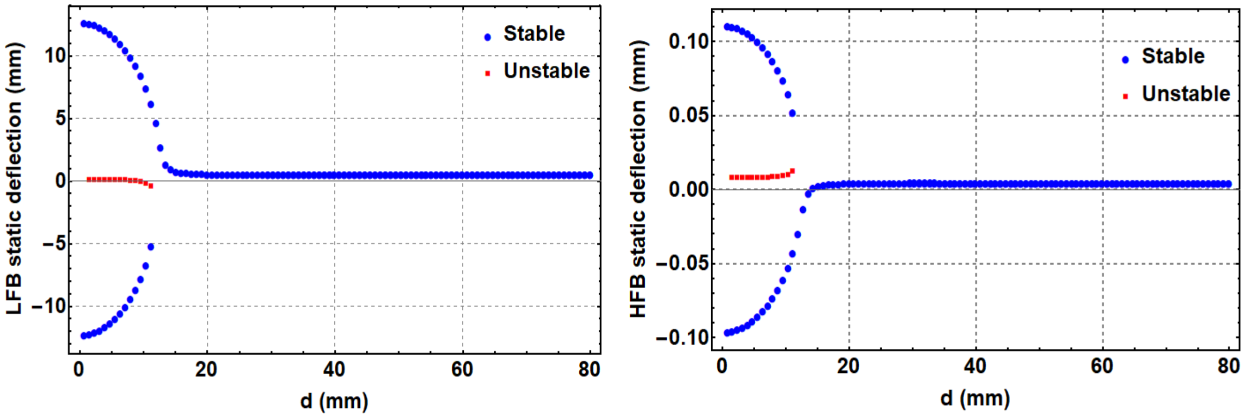

(a) (b)

Figure 3.4. Simulated static response for the center of the tip magnets as a function of the distance between the two magnets (d): (a) Static response of the LFB, (b) Static response of the HFB. Threshold distance (d_{th}) is found to be 15 mm for both tip magnets.

Dynamic Analysis

Figure 3.5 shows the frequency response curves of the LFB and HFB at a low excitation level of $0.05g$ excluding the magnetic effect. As shown in Fig. 3.5a, the natural frequency of the LFB is found to be 24 Hz, while the natural frequency of the HFB is found to be at 256 Hz as shown in Fig. 3.5b. In addition, the corresponding generated voltage of the HFB is shown in Fig. 3.5c, and found to have a maximum voltage of 0.36 V.

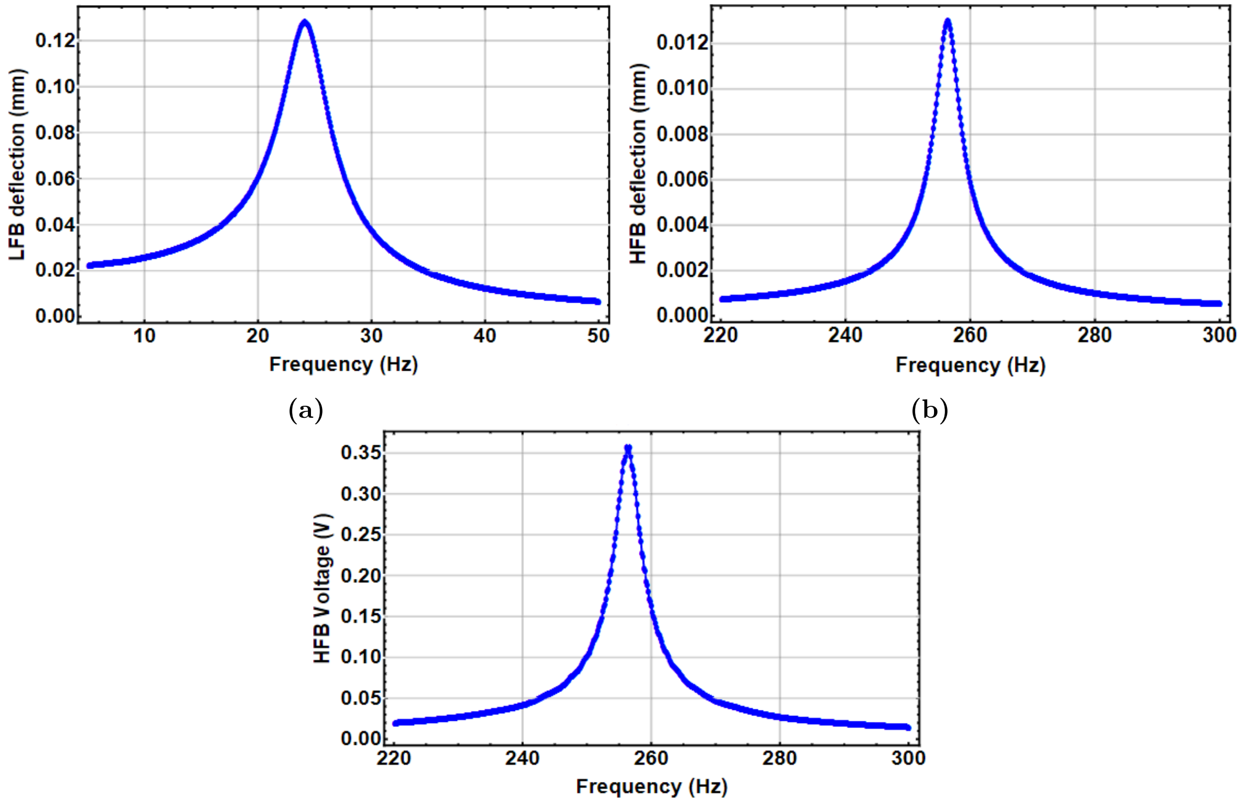

(a) **(b)**

(c)

Figure 3.5. Frequency response curves for the LFB and HFB at excitation of 0.05 g and without magnetic effect: (a) LFB frequency response curve, (b) HFB frequency response curve. (c) The voltage response curve of the HFB at excitation of 0.05 g without magnetic effect.

Figure 3.6 shows the voltage response curve of the HFB at different excitation levels and with a wide frequency range that covers both LFB and HFB natural frequencies. The separation distance between the two magnets was set to $d = 20\ mm$, which is larger than the threshold distance of the system, so the oscillation happens at the monostable region. According to Fig. 3.6a, by increasing the excitation level, the maximum generated output voltage increases until reaching 11 V at 1.5 g, and this can be related to higher stress and strain developed on the piezoelectric layers with higher excitation. Zooming into the range of frequencies around the LFB's natural frequency, it is noticed that a new voltage signal is created at 24 Hz as shown in Fig. 3.6b. This generated voltage at 24 Hz proves the frequency up-conversion effect. This peak is generated due to the magnetic coupling force between the two beams' tip magnets, known as the frequency up-converter effect since the piezoelectric laminates on the HFB generate a voltage at the LFB natural frequency. It is also seen that the effect of increasing the excitation level on amplifying the generated voltage signal where it reaches 0.2 V at 1.5 g.

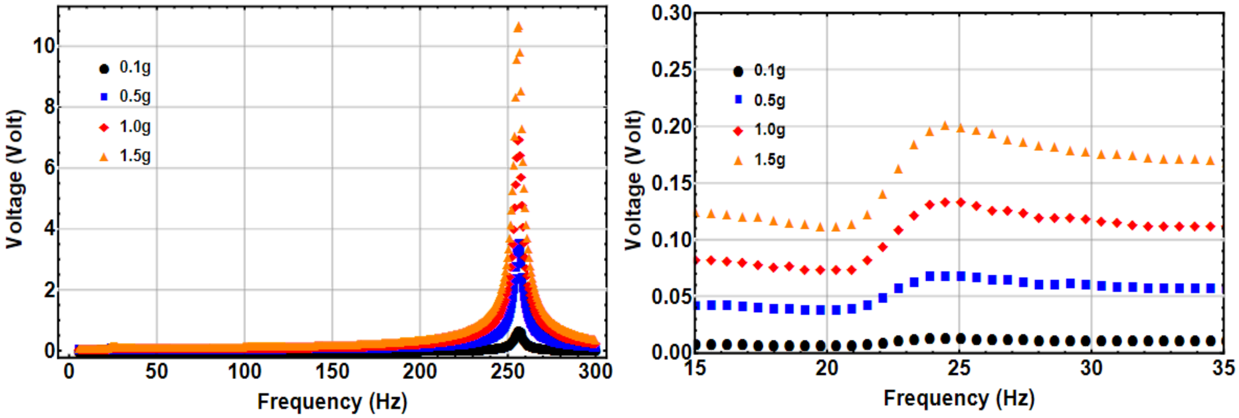

(a) **(b)**

Figure 3.6. The voltage response curve of the HFB at different excitation levels and 20 mm separation distance: (a) Voltage response over a full frequency range, (b) Voltage response of the HFB at the LFB frequency range.

In Fig. 3.7a, the separation distance between both magnets, d, is decreased to 15 mm, which equals the threshold distance, so the beam is vibrating at the threshold region. The frequency at this separation distance is shifted to a lower value of 18.5 Hz compared to 24_Hz at 20 mm separation distance shown in Fig 3.6b. In Fig. 3.7a, the hardening phenomenon is noticed when increasing the excitation level because the positive cubic nonlinearity in the magnetic force dominates at the threshold. Also, the voltage reaches a maximum value of 0.42 V at 1.5 g excitation level. Compared to the monostable case at 20 mm separation distance, the higher output voltage is achieved at the threshold distance is related to the higher magnetic coupling between the two beams at a lower separation distance. Lowering the separation distance between the two magnets to the bistable region results in shifting the frequency up to 41.0 Hz for the nonlinear harvester compared to the linear at 24.0 Hz as shown in Fig. 3.7b. Furthermore, increasing the excitation level results in a nonlinear softening behavior because the quadratic nonlinearity from the magnetic force dominates at the bistable region, as shown in Fig. 3.7b. The generated output voltage increases by increasing the excitation level and reaches a maximum value of 1.2 V, which is equivalent to 192% and 500% increment compared to the threshold and monostable regions, respectively. Next, the effect of the resistance on the generated voltage in the bistable region ($d = 8\ mm$) has been investigated. By varying the resistance from 100 $k\Omega$ to 100 $M\Omega$ at $1g\ level$, the generated voltage increases with increasing the resistance up to 10 $M\Omega$, where no further increment can be noticed even at higher resistances as shown in Fig. 3.8. At 10 $M\Omega$ or higher, a maximum voltage of 0.8 V is generated.

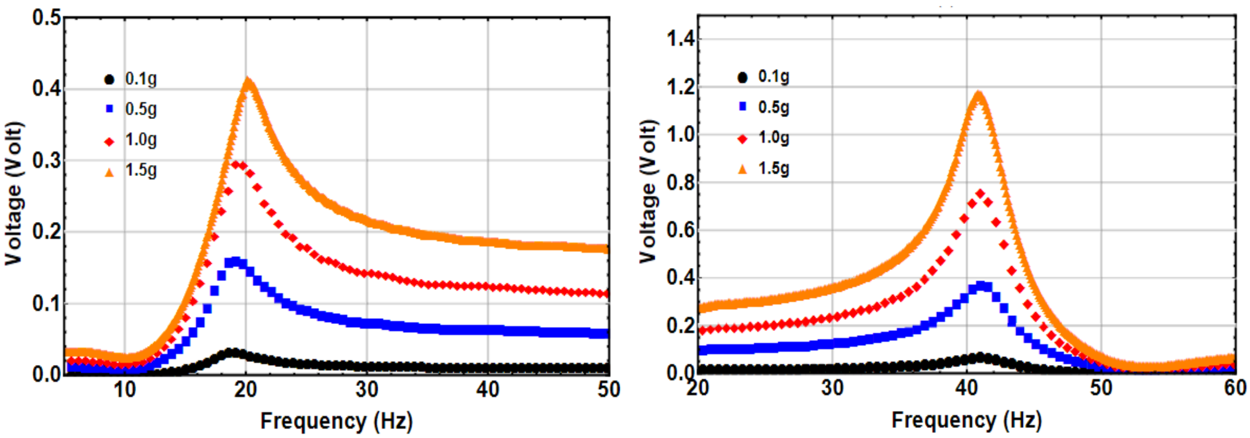

(a) **(b)**

Figure 3.7. The voltage response curve of the HFB at different excitation levels: (a) 15 *mm* separation distance, (b) 8 *mm* separation distance.

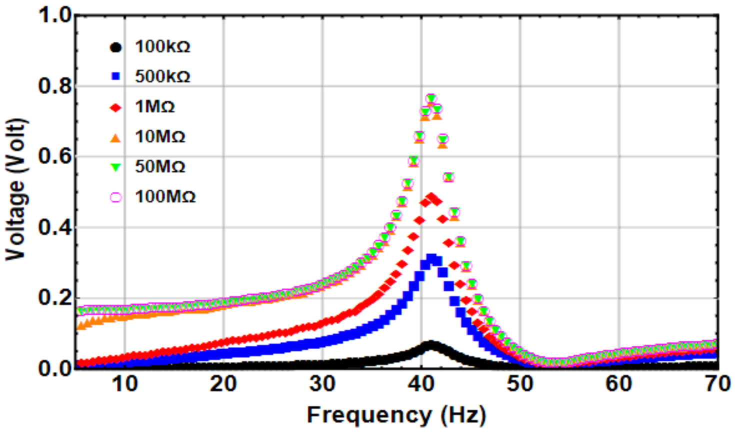

Figure 3.8. The voltage response curve of the HFB at different resistance R, and 8 *mm* separation distance, and at 1.0 g excitation level.

Experimental Validation

In this section, the theoretical model will be validated experimentally.Toward this, the theoretical model is modified to accommodate the experimental geometrical and physical parameters. The beams are attached to a holder, and the whole setup is installed on an electrodynamics shaker as shown in Fig. 3.9a. Compare to the previous structure, the only major changes was the HFB, where it is designed to be a unimorph beam (One piezoelectric strip attached to the top surface of the beam). The theoretical model is exactly as discussed previously, however, the equivalent moment of inertia of the HFB and piezoelectric strip is now different and can be calculated using Eqn. 3.7 [106].

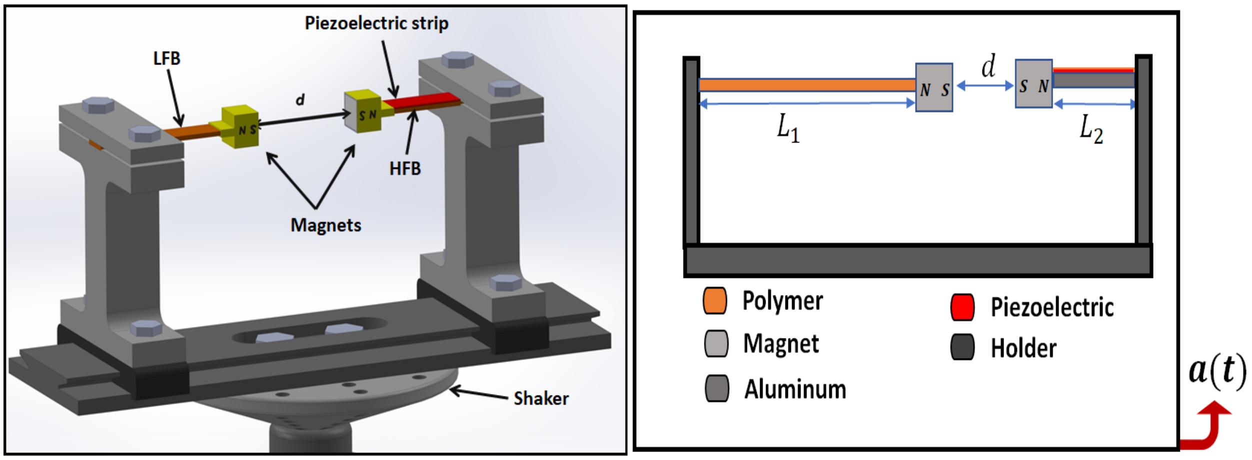

(a) **(b)**

Figure 3.9. 3D model and schematic of the system. (a) A 3D model of the system. (b) A schematic of the system.

$$I_{eq} = \frac{W_p t_p^3}{12} + (t_p W_p (t_h + \frac{t_p}{2}) - Y_n)^2 + \frac{n W_p t_h^3}{12} + t_h n W_p (\frac{t_h}{2} - Y_n)^2 \tag{3.7}$$

Where Y_n is the location of the neutral axis of the HFB with the piezoelectric strip and can be calculated using Eqn. 3.8. Also, t_p and t_h are thicknesses of the piezoelectric strip and the HFB, respectively. W_p represents the width of the piezoelectric strip, and n is the ratio of the modulus of elasticity of the HFB to the modulus of elasticity of the piezoelectric strip ($n = \frac{E_h}{E_p}$).

$$Y_n = \frac{(\frac{t_p}{2} + t_h)t_p + (\frac{t_h}{2})n t_h}{(t_p + t_h n)}. \tag{3.8}$$

By evaluating the neutral axis location, Y_n, the Electro-mechanical coupling factor, θ, can be calculated as:

$$\theta = d_{31} \left(\frac{k_2 b_2 L_2 (L_2 + L_p) Y_n}{2 I_{eq}} \right) \tag{3.9}$$

Where d_{31} is the Piezo Strain Constant. Also, b_2 and L_p are the width of the HFB and the length of the piezoelectric strip, respectively. The final form of the governing equations will be

$$
\begin{aligned}
&m_1\ddot{z}_1(t) + c_1\dot{z}_1(t) + k_1 z_1(t) + F_{magy} = m_1 a(t) \\
&m_2\ddot{z}_2(t) + c_2\dot{z}_2(t) + k_2 z_2(t) + \theta v(t) - F_{magy} = m_2 a(t) \\
&\dot{v}(t) - \chi\dot{z}_2(t) + \lambda v(t) = 0
\end{aligned}
\tag{3.10}
$$

Experimental Setup

The experimental setup used in this study is shown in Fig. 4.2. The setup consists of the VR9500 control unit, amplifier, electrodynamic shaker, and energy harvesting structure. The control unit controls the amplitude and frequency of the base excitation that the shaker will apply. The amplifier receives the signal from the control unit then it sends it to the shaker. Once the shaker receives the signal from the amplifier, it starts shaking. The structure of the beams is installed on the shaker so that it will oscillate under the base excitation. The frequency response curves of the LFB and HFB beams are measured by accelerometers attached to the tip of each beam. The accelerometers are connected to the VR9500 control unit and measure the deflection of the beams, and they are plotted versus the applied frequency. Also, the voltage is generated by a piezoelectric strip attached to the HFB. When the beam oscillates, its deflection develops stress and strain on the piezoelectric strip, so the voltage is generated, then measured and recorded by the controller.

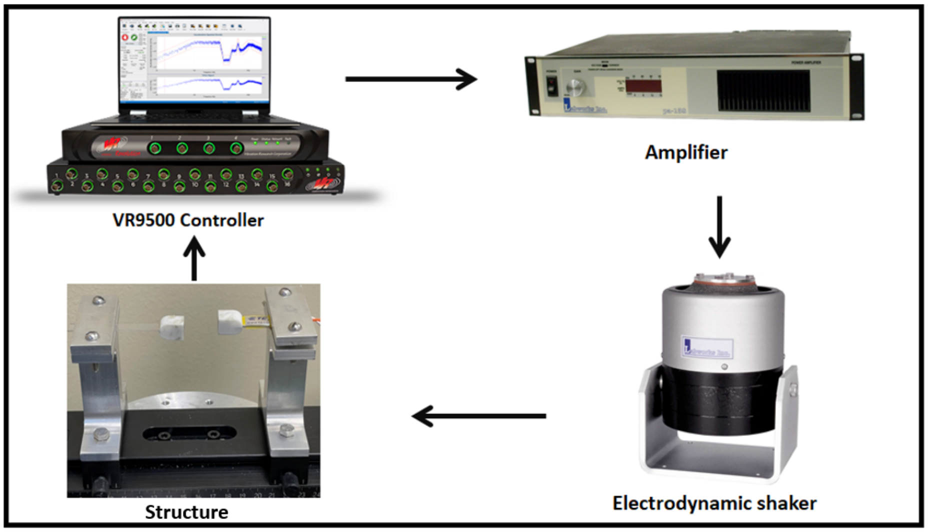

Figure 3.10. Experimental setup used to test the piezoelectric energy harvester.

Using the geometrical parameters listed in Table. 3.2, the static solution can be extracted. Figure 3.11 a and b show the static response of the LFB and HFB, respectively, with the variation of the horizontal distance between the two tip magnets. It is clearly shown that a critical threshold separation distance of $d_{th} = 15mm$. This threshold distance divides the system into two main parts, a monostable region where $(d > d_{th})$ and a bistable region where $(d < d_{th})$. The static experimental measurements were conducted manually using a ruler for the LFB, and the experimental and simulated static results are in excellent agreement with each other.

Table 3.2. Modified physical and geometrical parameters to be used in the model.

Parameters	**Symbol**	**Value**
LFB (length $\times$*width* $\times$ *thickness*)	$L_1 \times b_1 \times h_1$	$(26 \times 10 \times 1)$ mm
LFB Young's modulus	E_1	2.344 Gpa
LFB Density	ρ_1	1220 $\mathrm{kg/m^3}$
LFB Damping coefficient	c_1	0.0038 N.s/m
HFB (length $\times$*width* $\times$ *thickness*)	$L_2 \times b_2 \times h_2$	$(19 \times 10 \times 1.6)$ mm
HFB Young's modulus	E_2	69.0 Gpa
HFB Density	ρ_2	2700 $\mathrm{kg/m^3}$
HFB Damping coefficient	c_2	0.38 N.s/m
Piezoelectric (length $\times$*width* $\times$ *thickness*)	$L_p \times b_p \times h_p$	$(40 \times 7 \times 0.02)$ mm
Piezoelectric Young's modulus	E_p	2450 Mpa
Piezoelectric Density	ρ_p	1780 $\mathrm{kg/m^3}$
Resistance	R	200 kΩ
Magnets side length	L_m	8.0 mm
Magnetic moment	$q_1 = q_2$	0.5 A^2/m
Piezo Strain Constant	d_{31}	23×10^{-12}
Piezoelectric Laminate permittivity	ϵ_{33}	$3250 \times 8.854 \times 10^{-12}$

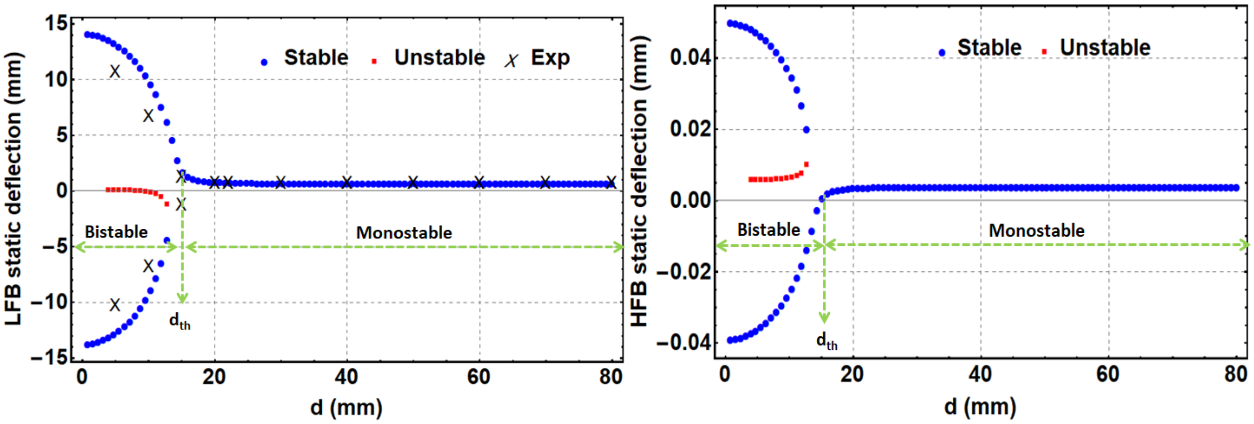

(a) (b)

Figure 3.11. The static response of the LFB and HFB versus the separation distance. (a) Experimental and Theoretical response of the LFB. (b) Theoretical response of the HFB. Threshold value, d_{th}, found to be $15mm$. The monotstable, threshold, and bistable are selected for the analysis.

Dynamic Analysis

Natural frequencies:

To solve for the natural frequencies of the system as a function of the separation distance, the total deflection of the beams was assumed to be a function of the static and dynamic deflections as:

$$\begin{aligned} z_1(t) &= u_1 + z_{1s} \\ z_2(t) &= u_2 + z_{2s} \end{aligned} \tag{3.11}$$

Where u_1 and u_2 are the dynamic deflections for the LFB and HFB, respectively. Accordingly, the total vertical deflection will be:

$$Y = Y_s + Y_u. \tag{3.12}$$

Where $Y_s = z_{1s} + z_{2s}$ and $Y_u = u_1 + u_2$. By substituting Eqn.(3.12) in the vertical magnetic force (F_{magy}), Eqn.(3.4), it will be:

$$F_{magy} = \frac{F_R(Y_s + Y_u)}{(d^2 + (Y_s + Y_u)^2)^{5/2}} \tag{3.13}$$

Substituting equations (1-12) into Eqn.(3.10), will result the following governing equation:

$$
\begin{aligned}
&m_1\ddot{u}_1(t) + c_1\dot{u}_1(t) + k_1(u_1 + z_{1s}) + F_{magy} = m_1 a(t) \\
&m_2\ddot{u}_2(t) + c_2\dot{u}_2(t) + k_2(u_2 + z_{2s}) + \theta v(t) - F_{magy} = m_2 a(t) \\
&\dot{v}(t) - \chi\dot{u}_2(t) + \lambda v(t) = 0
\end{aligned}
\tag{3.14}
$$

Where m_1, c_1, and k_1 are the equivalent mass, damping coefficient, and the stiffness of the LFB, respectively, while m_2, c_1, and k_2 are the equivalent mass, damping coefficient, and the stiffness of the HFB. To benefit from the static equations (Eqn. (3.5) and (3.5)), and avoid the complications of the magnetic formula in getting the numerical solution, the magnetic force, F_{magy}, was expanded using Taylor's series around zero dynamic deflection ($Y_u = 0$). Accordingly, the magnetic force will be:

$$
F_{magy} = \frac{F_R Y_s}{(d^2 + Y_s^2)^{5/2}} + \frac{F_R(d^2 - 4Y_s^2)}{(d^2 + Y_s^2)^{7/2}} Y_u = F_{magys} + F_{magyu} \tag{3.15}
$$

Where F_{magys} and F_{magyu} represent the static and linearized dynamic magnetic force, respectively, and Y_u is the dynamic deflection. To improve the results, the magnetic force was expanded up to nine terms using Taylor's series so the new terms of the dynamic magnetic force will be:

$$F_{magyu} = \sum_{i=1}^{9} \alpha_i Y_u^i(t), \qquad i = 1, 2, ...9 \tag{3.16}$$

Where $\alpha_1, \alpha_2, ..., \alpha_9$ are the coefficients of Taylor's series expansion of the dynamic magnetic force, listed in the Appendix. When Eqn. (3.16) is substituted in Eqn. (3.14), the static terms will cancel each other, therefore the governing equations of the system will be:

$$\begin{aligned}
&m_1\ddot{u_1}(t) + c_1\dot{u_1}(t) + k_1u_1 + F_{magyu} = m_1a(t)\\
&m_2\ddot{u_2}(t) + c_2\dot{u_2}(t) + k_2u_2 + \theta v(t) - F_{magyu} = m_2a(t)\\
&\dot{v}(t) - \chi\dot{u_2}(t) + \lambda v(t) = 0
\end{aligned} \tag{3.17}$$

Now, by re-substituting the dynamic magnetic force of Eqn.(3.16) in Eqn.(3.17), and using $Y_u = u_1 + u_2$, the nonlinear natural frequencies of the system of the LFB and HFB, respectively, can be calculated as follows:

$$f_1 = \frac{1}{2\pi}\sqrt{\frac{k_1 + \alpha_1}{m_1}}, \quad f_2 = \frac{1}{2\pi}\sqrt{\frac{k_2 - \alpha_1}{m_2}}. \tag{3.18}$$

Where the term α_1 is the coefficient of the linear term after expansion the magnetic force with Taylor's series and given by:

$$\alpha_1 = \frac{F_R(d^2 - 4Y_s^2)}{(d^2 + Y_s^2)^{7/2}} \tag{3.19}$$

Using Eqn.(3.18), the variation of the natural frequencies of the LFB and HFB with the separation distance between the two magnets is extracted and shown in Fig. 3.12a and 3.12b, respectively. Also, the experimental variation of the natural frequencies with separation distance is recorded at $0.1g$ excitation level and reported for the LFB as shown in Fig. 3.12a. Both experimental and simulated results are in a great match for the LFB. Both plots show a threshold separation distance of $15mm$, which matches the same value calculated from the static results shown in Fig. 3.11. Also, Fig. 3.12 shows that at a high separation distance, the magnetic force becomes weak, and the natural frequencies match the linear values of both beams. Lowering the separation distance toward the threshold, the natural frequency of the LFB drops to reach a minimum value of $12Hz$. In contrast, the natural frequency of the HFB reaches its maximum value of $263.2Hz$. Decreasing the separation distance more to reach the bistable range will increase the natural frequency of the LFB to reach $43Hz$ and decrease the natural frequency of the HFB to reach $261.4Hz$. This difference in the change of the natural frequency between the LFB and HFB is due to the fact that the contribution of the magnetic force term (α_1) in Eqn.(3.19) changes its sign according to the value of d which results in lowering or increasing the natural frequency value. It is also noted that the variation of the natural frequency in the LFB is much more considerable than the HFB, which is due to the low stiffness material of the LFB (Polymer) compared to the HFB material (Aluminum).

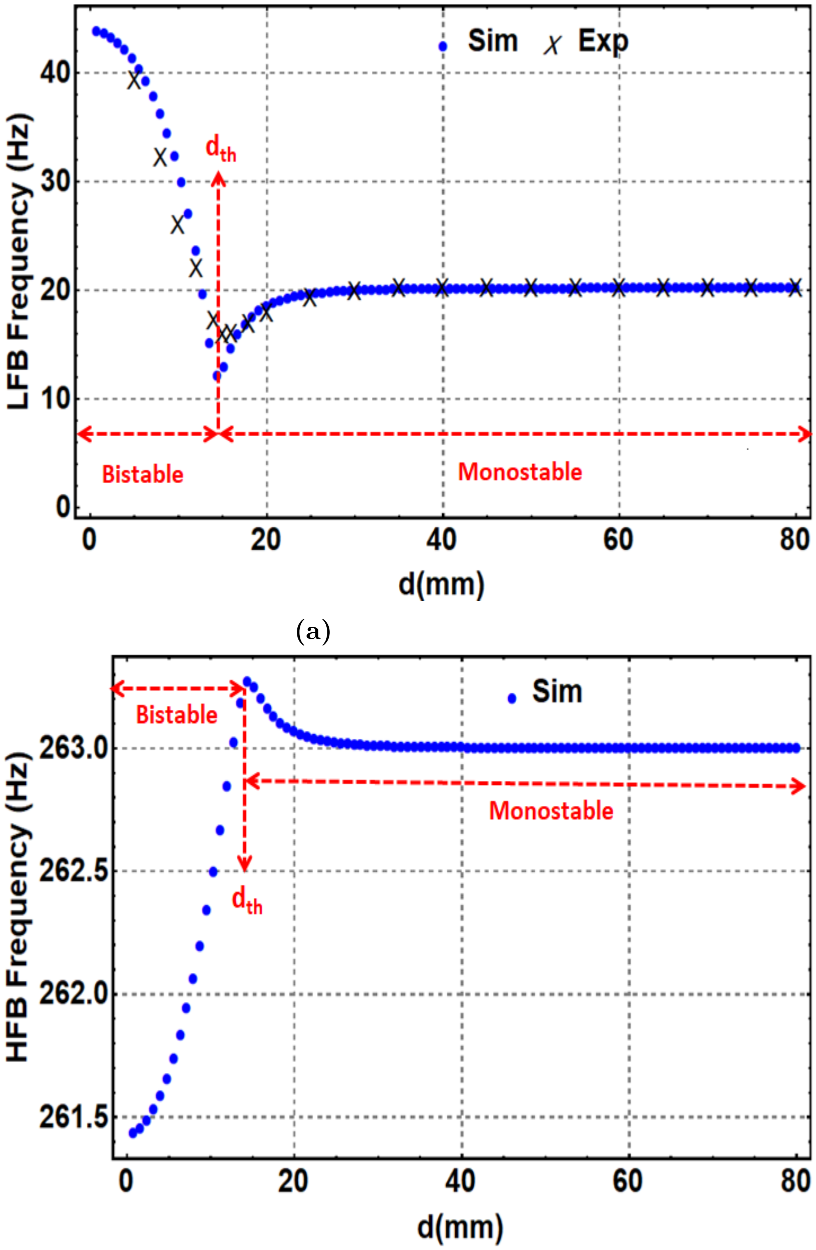

(a)

(b)

Figure 3.12. The natural frequency of the LFB and HFB with variable separation distance at $0.1g$. (a) LFB (b) HFB.

Linear Analysis:

The linear response of the system and the generated voltage can be investigated by eliminating the effect of the magnetic nonlinearity ($F_{magy} = 0$). Figure. 3.13 summarizes the simulated and experimental frequency response curves of the LFB, HFB, and the voltage repose curve at a low excitation level of $0.05g$. Figure. 3.13a represents the frequency response curve of the LFB, theoretical and experimental. From the figure, it is clear that the LFB's simulated and experimental natural frequency is at $20.8Hz$ with $2.75mm$ for the maximum deflection. Similarly, Fig. 3.13b shows the simulated and experimental natural frequency of the HFB is at $263Hz$ with $5.55 \times 10^{-3}mm$ maximum deflection. Additionally, Fig. 3.13c represents that voltage response curve that is generated from the piezoelectric layer. The figure shows that the voltage value peaked approximately at $263Hz$ with $5.9mV$ as a maximum generated voltage for the simulation and experiment. The maximum voltage is expected to be at $263Hz$ because the piezoelectric strip is attached to the HFB. When the HFB reaches the resonance, the maximum deflection will occur, which means applying higher stress and strain to the piezoelectric strip. Therefore, the highest voltage will be generated at the resonance of the beam.

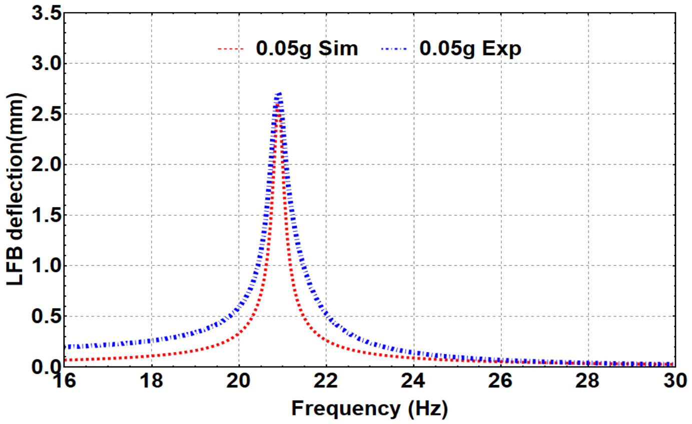

(a)

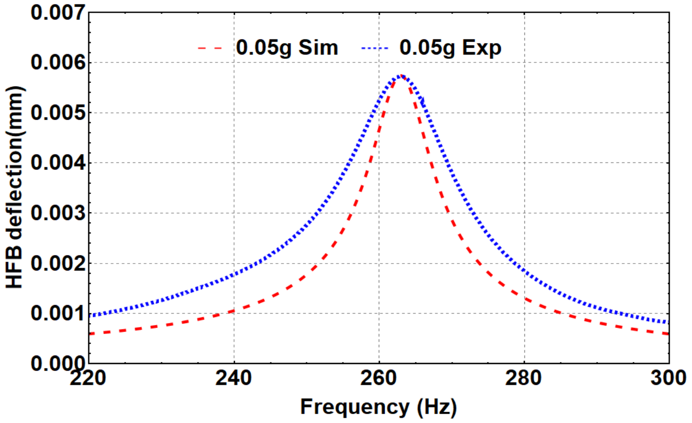

(b)

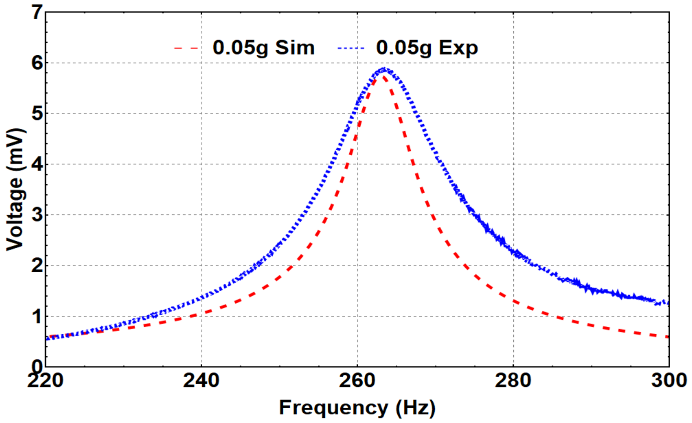

(c)

Figure 3.13. Frequency response curves of the LFB and HFB, and voltage response curve at $0.05g - level$. (a) LFB response curve. (b) HFB response curve. (c) Voltage response curve.

Nonlinear Analysis:

The system dynamics have been investigated at the three regimes, monostable, threshold, and bistable. A separation distance of $35mm$ and $15mm$ are selected for the monostable and threshold regions. For the bistable, values of $8mm$ and $5mm$ have been explored. At the three regimes, the generated voltage has been studied to show the frequency up-converter concept where the voltage will be generated at the LFB frequency range while the piezoelectric layer is attached to the HFB, and this is due to the magnetic coupling between both beams. At the monostable range ($35mm$), the system is excited at different excitation levels, as shown in Fig. 3.14d. Even though the piezoelectric strip is attached to the HFB, the voltage signal is generated at the LFB frequency range, proving the frequency up-converting concept due to the magnetic coupling. Also, it is noted that higher output voltage is generated at higher excitation levels. Furthermore, a nonlinear hardening behavior is shown with increasing the excitation level. Figure. 3.14e shows that the simulated results are in good agreement with the experimental results at $0.1g$ and $0.5g$ excitation levels.

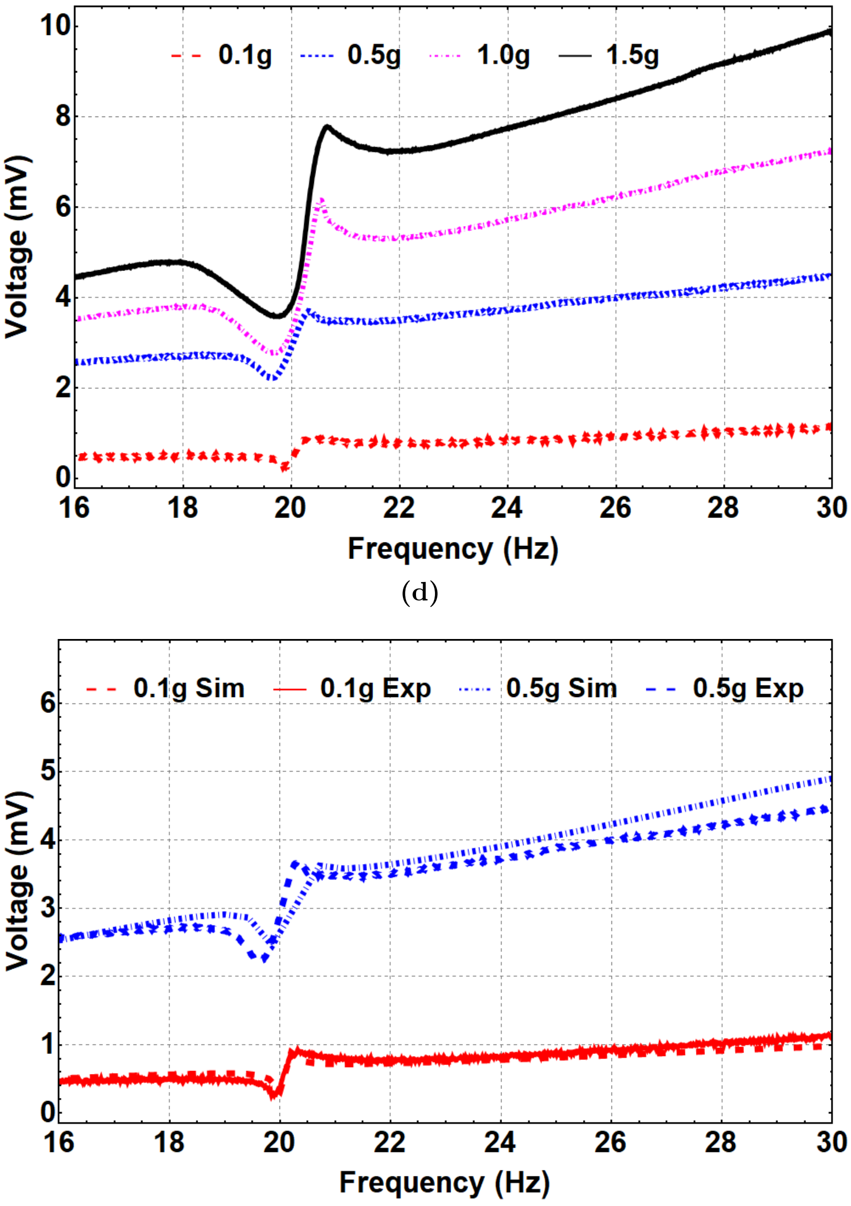

(d)

(e)

Figure 3.14. The generated voltage of the HFB at $d = 35mm$ at the LFB frequency range at different excitation levels. (a) Experimental results. (b) Experimental and simulated results.

Next, the system's dynamic behavior in the bistable range has been investigated. Toward this, the system is excited at different excitation levels for $8mm$ separation distance, as represented in Figure. 3.15. A hardening behavior is shown where the natural frequency is shifted to reach $30Hz$ compared to $20.8Hz$ for the linear harvester. This shift is due to the dominance of the cubic nonlinearity. By increasing the excitation levels, the quadratic nonlinearity becomes dominant, and a softening behavior shows up, as shown in Figure. 3.15b. Moreover, the generated voltage in the bistable range significantly increased to reach $52mV$ compared to $6mV$ for the monostable range at the $1.0g$ excitation level. The simulated results for selected excitation levels are in a good agreement with the experimental results, as shown in Figure. 3.15b.

Another separation distance was investigated in the bistable regime, where $d = 5mm$. Similarly, the system is excited at different excitation levels, as shown in Figure. 3.16. At $0.1g$, the natural frequency increased to $37.2Hz$ as shown in Figure. 3.16a, compared to $20.8Hz$ for the linear harvester. As reported previously, this increment is due to the dominance of the cubic nonlinearity at low excitation levels. At this separation distance, the natural frequency increased more than at $d = 8mm$ for the same excitation level and bistable range. This can be related to the higher coupling at a lower separation distance between identical tip magnets of both beams due to higher magnetic force. When the excitation level goes higher, a softening behavior is noticed, and it is significant compared to the previous

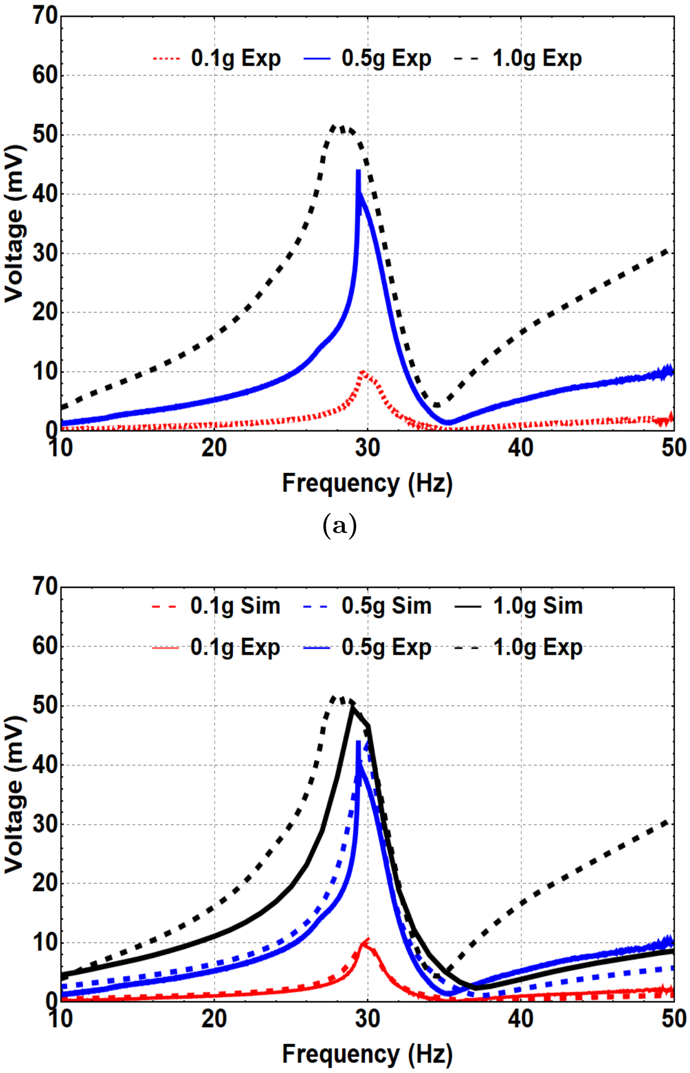

(a)

(b)

Figure 3.15. The generated voltage of the HFB at $d = 8mm$ at the LFB frequency range at different excitation levels. (a) Experimental results. (b) Experimental and simulated results.

one at $d = 8mm$. Also, the amplitude of the generated voltage raised significantly to reach around $170mV$ at $1.5g$. The match between the experimental and simulated generated voltage at $0.1g$ and $0.5g$ is presented in Fig. 3.16b. The plot shows the agreement between the results, which credits the validity of the model and the previous results.

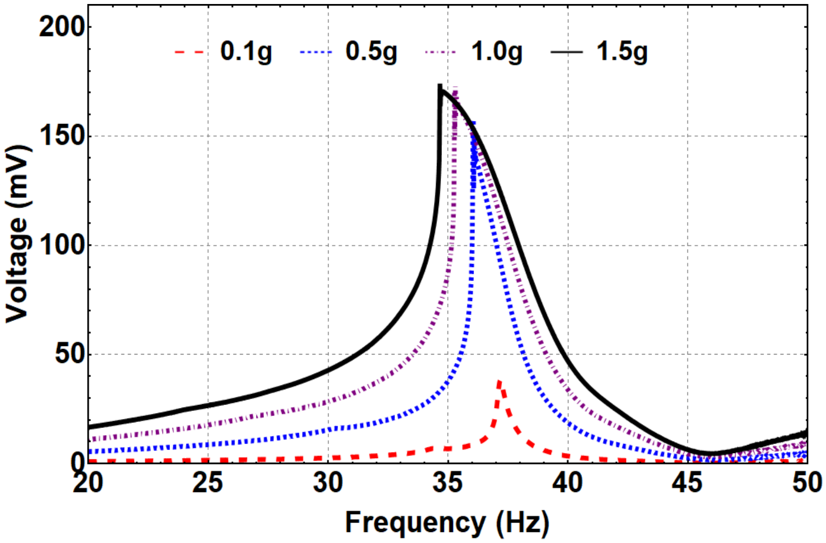

(a)

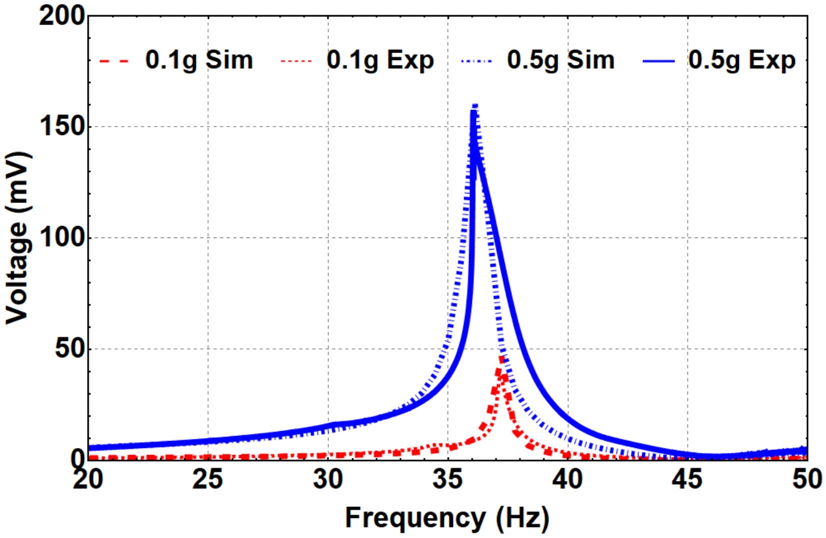

(b)

Figure 3.16. The generated voltage of the HFB at $d = 5mm$ at the LFB frequency range at different excitation levels. (a) Experimental results. (b) Experimental and simulated results.

After that, the threshold region is investigated. Figure. 3.17 shows the experimental and simulated generated voltage at the threshold regime at $d_{th} = 15mm$. The system response of this region was investigated at different excitation levels. At $0.1g$, the natural frequency dropped to $17Hz$ showing a softening behavior, compared to $20.8Hz$ for the linear harvester. Opposite to the bistable, the quadratic nonlinearity dominates at low excitation levels at the threshold, so the natural frequency decreases, as shown in Fig. 3.17a. Also, it is noted that by increasing the excitation level, the natural frequency starts to increase after $0.5g$, so a nonlinear hardening behavior starts taking place. This combined softening and hardening behavior can be related to the dominance change of the quadratic nonlinearity at low excitation levels to the cubic nonlinearity at higher excitation levels at the threshold regime. Figure. 3.17b shows the simulated generated voltage at different excitation levels for the same separation distance. Qualitatively, the simulated results show that at $0.5g$, the behavior starts to change from softening to hardening at higher excitation levels. Also, Fig. 3.12a shows that the experimental natural frequency at $d_{th} = 15mm$ is approximately $17Hz$, while it is around $12Hz$ for the simulated natural frequency at the same separation distance at $0.1g$. This finding is in agreement with experimental and simulated natural frequency at $0.1g$ in both figures, Fig. 3.17a and 3.17b. Compared with the monostable region, the threshold plots show higher generated voltage for both simulation and experiment. At $0.1g$, the experimentally generated voltage recorded $1mV$ in the monostable, while it reached $2mV$

at the threshold, which is 100% higher. Also, the $0.8g$ in the experimental results at the threshold peaked at almost $22mV$, which is higher than the $1.5g$ in the monostable that maximized at $8mV$. This higher generated voltage at the threshold can be related to the higher coupling generated by decreasing the separation distance.

The effect of the external resistance variation on the maximum output voltage has been investigated too. Figure. 3.18 shows the change of the maximum output voltage with changing the external resistance of the system at the bistable range $d = 5mm$ at $0.5g$. The $200k\Omega$ was used in this study so far, and as shown the Fig. 3.18, the maximum output voltage at this resistance value is approximately $0.16V$, and that was reported previously in Fig. 3.16b. By decreasing the resistance to $100k\Omega$, the voltage was reduced to roughly $0.09V$. When the resistance started to increase over $200k\Omega$, the amount of the produced voltage also increased. At resistance equals $1M\Omega$, the voltage went up to $0.7V$, then approximately doubled to reach $1.12V$ at $2M\Omega$. For the $25M\Omega$, the produced voltage recorded $2.0V$. With further resistance increase, the voltage does not go up, where the $50M\Omega$ produced $2.0V$. Therefore, the maximum output voltage can be obtained at resistance with $25M\Omega$.

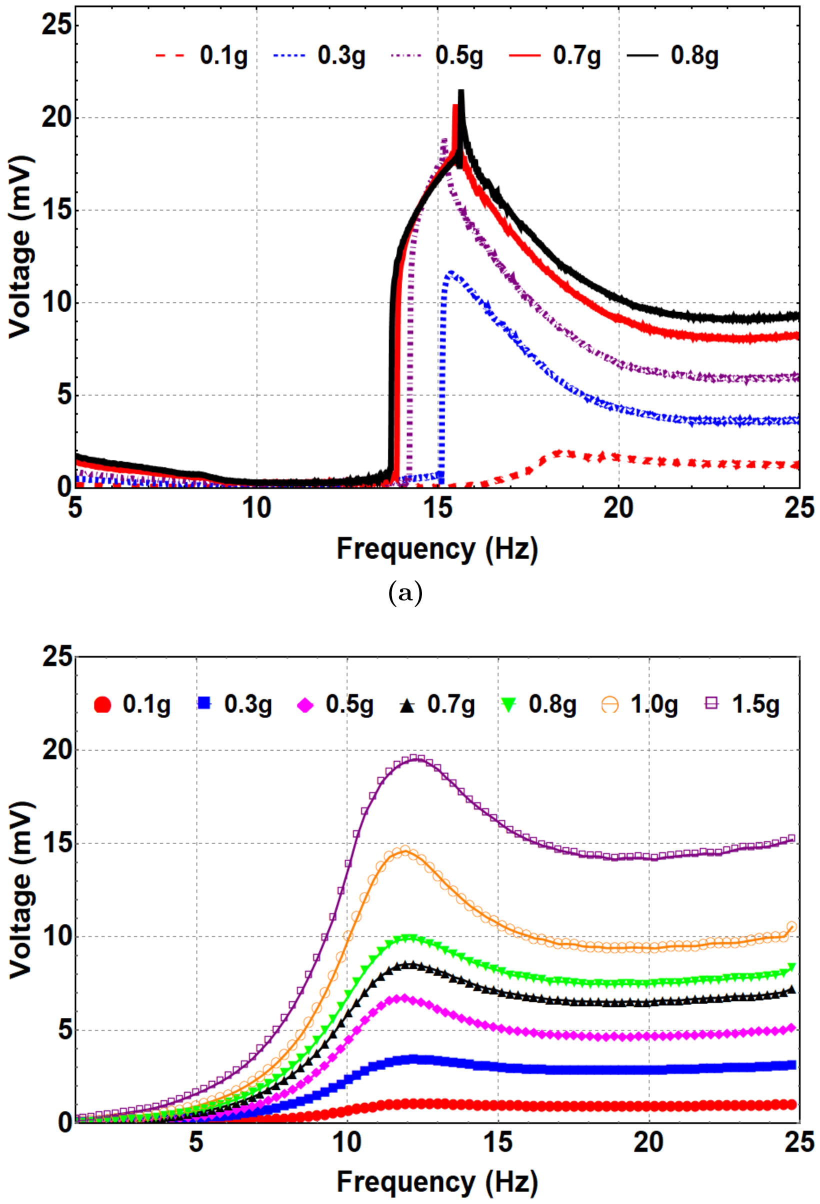

(a)

(b)

Figure 3.17. The generated voltage of the HFB at $d = 15mm$ at the LFB frequency at the LFB frequency range at different excitation levels. (a) Experimental generated voltage. (b) Simulated generated voltage.

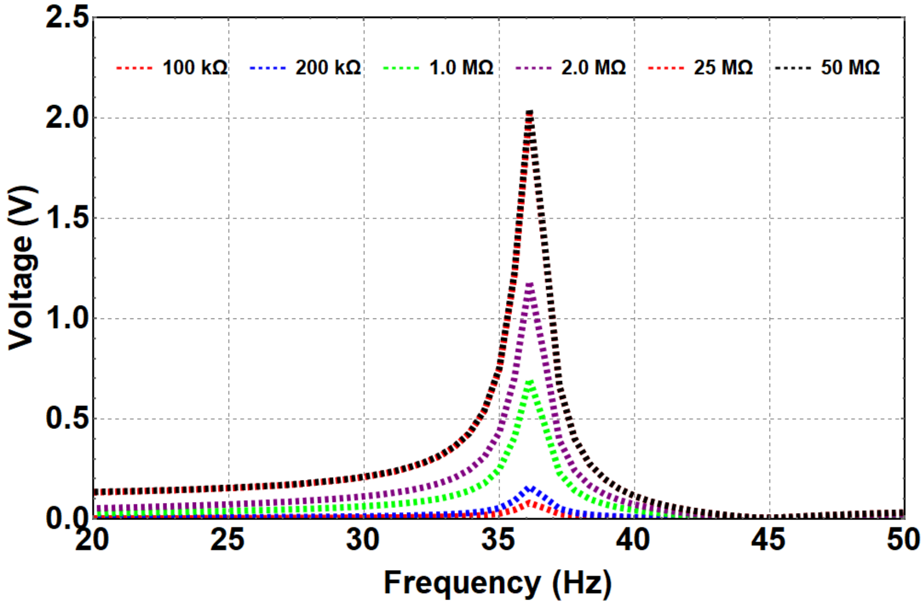

Figure 3.18. Maximum output voltage with increasing the resistance to $50M\Omega$ at separation distance equals to $5mm$ at $0.5g - level$.

Chapter Four

Self-Powered Orthopedic Load Monitoring Systems

The orthopedic surgeries are considered one of the most common surgical operations worldwide. Joint replacement surgeries, such as TKR and THR, are one of these common surgeries that happen because joints wear out from Osteoarthritis. To continuously monitor and increase the satisfaction level of these implants, TKR and THR, a novel study has been conducted and presented in this chapter by integrating the triboelectric energy harvester with these implants to be self-powered mechanisms that work postoperatively for load monitoring and performance improvement.

TKR Load Monitoring System

Two new configurations of a triboelectric energy harvester for TKR are investigated as they measure the knee loads under cyclic loading developed using a Dynamic Tester. The first configuration is a full knee harvester, while the second configuration is composed of two harvesters installed at the medial and lateral positions in the knee. Both configurations were placed between the Ultra-High-Molecular-Weight Polyethylene (UHMWPE) bearing and the tibial tray of TKR implants, allowing load sensing to be incorporated into any TKR system. Because of the significant effect of imbalanced loads on TKR performance, estimating these loads would improve the implant and provide critical data on stress distribution, its effect on both the harvester and the bones, and its effect on the interaction between the implant and the bones. [107]. Hence, comparing the performance of the proposed two configurations of the triboelectric generator under cyclic loading conditions would be a direct indicator of their ability to harvest and generate energy and sense load in the knee. The following parts include discussing the two proposed harvester configurations, followed by a description of the experimental setup to evaluate their performance. Results from the experimental work are discussed to draw conclusions and capture indicators for future work.

Triboelectric Generator Assembly

A schematic of the structure of a triboelectric energy harvester is shown in Fig. 4.1. Part (a) of the Figure shows that the harvester is composed of an upper patterned conductive aluminum layer, a lower conductive flat aluminum layer, and patterned polydimethylsiloxane (PDMS) insulator attached to the lower aluminum layer, with matching patterned surfaces (sawtooth ridges) to the upper layer. Both conductive and PDMS layers have a thickness of 1.00 mm. The two conductors are attached to 3D printed mold consisting of two parts,

Fig. 4.1d. The upper part represents the Ultra-High Molecular-Weight Polyethylene (UHMWPE), and the lower part represents the tibial tray of TKR implants. The mold parts are separated by mechanical springs at the corners. The upper conductor in each assembly will be attached to the upper mold part, and the lower conductors will be attached to the lower mold part. The external load will be applied to the upper mold part and transferred to the triboelectric harvesters. Part (b) of Fig. 4.1. shows the full knee harvester configuration, which has an area of 33.9 cm^2. Part (c) of Fig. 4.1 shows the combined lateral and medial harvester configuration where it has the area of 25.8 cm^2.

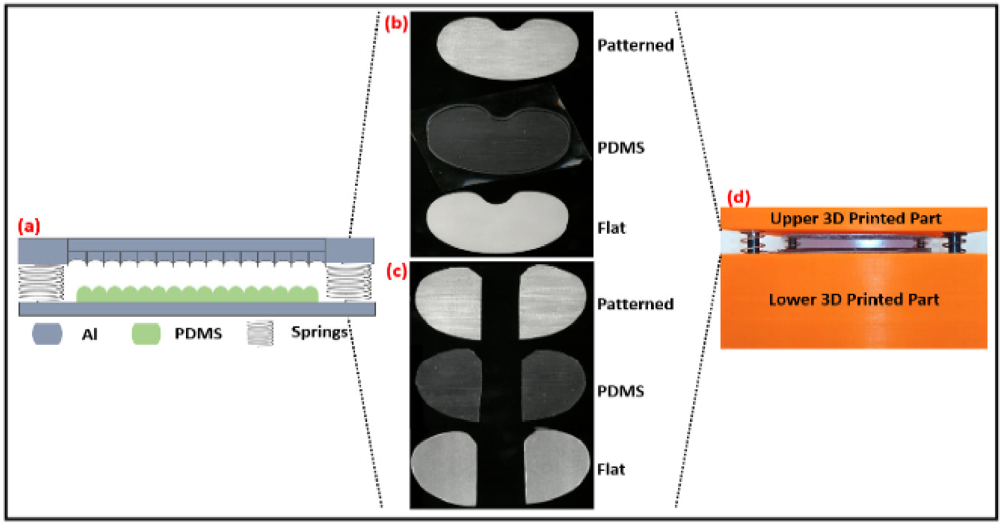

Figure 4.1. (a) Schematic for the structure of the triboelectric energy harvester. (b) Full knee configuration (c) lateral and medial configuration, (d) 3D printed mold.

Experimental Setup and Procedure

The experimental setup used in this study is shown in Fig. 4.2. The setup consists of a control unit, the dynamic tester, and a monitoring oscilloscope. The control unit controls the amplitude and frequency of the load applied by the dynamic tester to the harvester under testing. The dynamic tester is used to apply the force profile, enabling the evaluation of the triboelectric generator's performance. The applied force is measured with a load cell, while the generated voltage signal is measured and recorded using the oscilloscope. Experiments were conducted by subjecting each harvester configuration to a cyclic load using the dynamic tester. This cyclic load drives the contact and separation action between the harvester's two parts, eventually producing AC voltage. During the harvester loading part of the cycle, the upper Aluminum conductor comes in contact with the PDMS gaining a positive electric charge while leaving the PDMS with a negative electric charge. These charges are generated due to the triboelectrification effect stemming from the involved materials having different tendencies to lose and gain electrons. During the harvester unloading part of the cycle, the two harvester parts become out of contact due to the mechanical springs' reactions causing the electrons to move from one electrode to the other based on potential differences. Consequently, this causes a current flow. A charge balance occurs at the full separation between the two harvester parts, causing a current flow to stop. As the cycle of loading and unloading repeats, the two harvester parts start approaching each other again, causing electrons to flow in the reverse direction. Consequently, an alternating current is generated. Voltage resulting from electrons flow is captured and recorded by the oscilloscope, which has an internal resistance of 50 $k\Omega$.

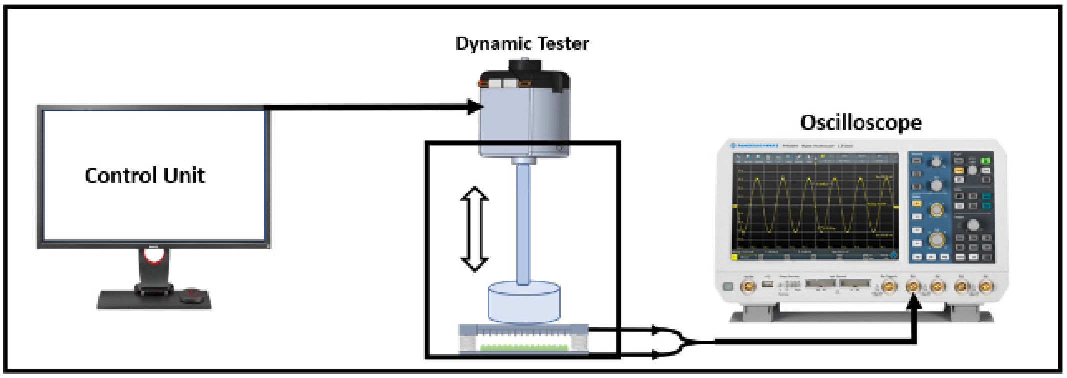

Figure 4.2. Experimental setup used to test the triboelectric harvesters.

Results and Discussion

The load transferred to the knee from different activities of daily living can range from 100 N to reach peak values of around 4000 N [108] depending on human body weight. The dynamic tester used in the reported experiments is limited by the amount of force applied. Therefore, the generators' performance is investigated under two different cyclic loads of 11.0 N and 24.0 N and at two different frequencies of 0.60 Hz and 1.20 Hz. Figure. 4.3 shows a sample of the cyclic load profile applied to both prototypes by the dynamic tester at 0.60 Hz. The magnitude of the force in Fig. 4.3 was set to 11.0N as the first trial to test both configurations' performance. The normal walking (gait) frequency is usually approximated to be at 1.0 Hz, but it differs from one person to the other depending on the human's age. Therefore, the effect of the frequency at 0.6 Hz and 1.2 Hz on the generated output was included in the investigation.

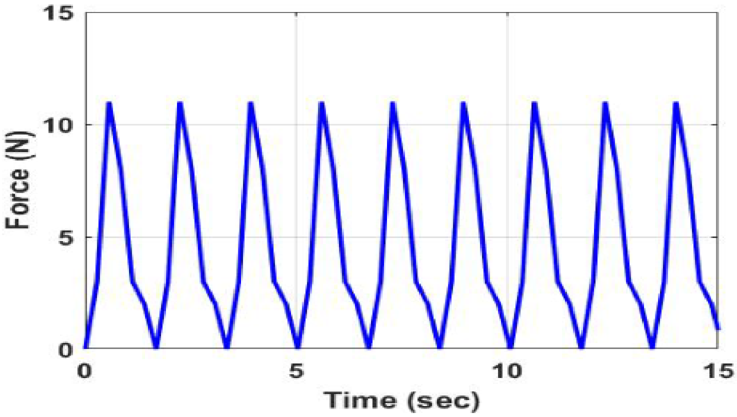

Figure 4.3. Sample of the cyclic load profile applied by the dynamic tester at 0.60 Hz.

Full Knee Configuration

The generated voltage results from testing the full knee harvester at 0.60 Hz and 1.20 Hz with applied load of 11.0 N are presented in Fig. 4.4a. The generated voltage at 0.60 Hz peaked at approximately 0.45 V and was almost consistent. However, at 1.20 Hz, the average voltage peak was 0.80 V with a variation of ±0.05 V. These results indicate that output voltage is directly proportional to the loading frequency. Moreover, a maximum corresponding generated voltage is reached when the triboelectric harvester layers start to separate and reach the minimum gait load at the full separation between the two layers. When the triboelectric layers start to contact each other, the generated voltage signal becomes smaller and drops to reach its minimum absolute value of zero at full contact. At this moment, the triboelectric and electrostatic charges stabilize. As the two harvester parts come out of contact, the voltage increases in the opposite direction to reach the maximum value at full separation. Therefore, we notice that the triboelectric effect works based on the continuous contact and separation action. The full knee configuration was also tested with the maximum load of 24.0 N at both frequencies of 0.60 Hz and 1.20 Hz. Figure. 4.4b shows the generated output voltage with a small increase compared to the output when 11.0 N was the applied load. Moreover, the voltage peaked at 0.55 V for 0.60 Hz and 0.95 V for 1.20 Hz. We notice an increment in the voltage output by 22.2 % at 0.60 Hz and 18.7 % at 1.20 Hz at 118 % increment in the applied load.

The generator's performance is investigated at the two different cycle loads of 11.0 N and 24.0 N, and the generated voltage amplitudes are shown in Fig. 4.4. The results demonstrate the proportionality of the generated voltage with the applied cyclic load. The higher voltage is generated at a higher applied load. This increase in the voltage output can be correlated to the higher penetration in the PDMS layer under a higher applied load, which results in a higher surface contact area. The results were demonstrated in bar plots to show that the output voltage rises by increasing the applied load from 11.0 N to 24.0 N, as shown in Fig. 4.5. This proportionality between the applied force and the voltage outputs is considered promising for powering load sensors and their telemetry circuitry for TKR applications.

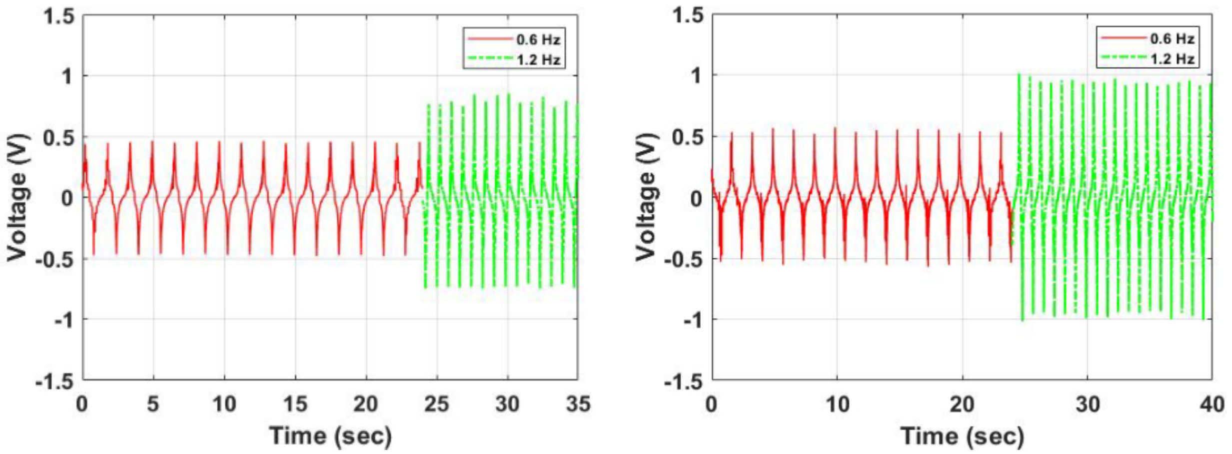

(a) **(b)**

Figure 4.4. Voltage output of the full knee harvester at 0.60 Hz and 1.20 Hz when loaded with: (a) 11.0 N, (b) 24.0 N.

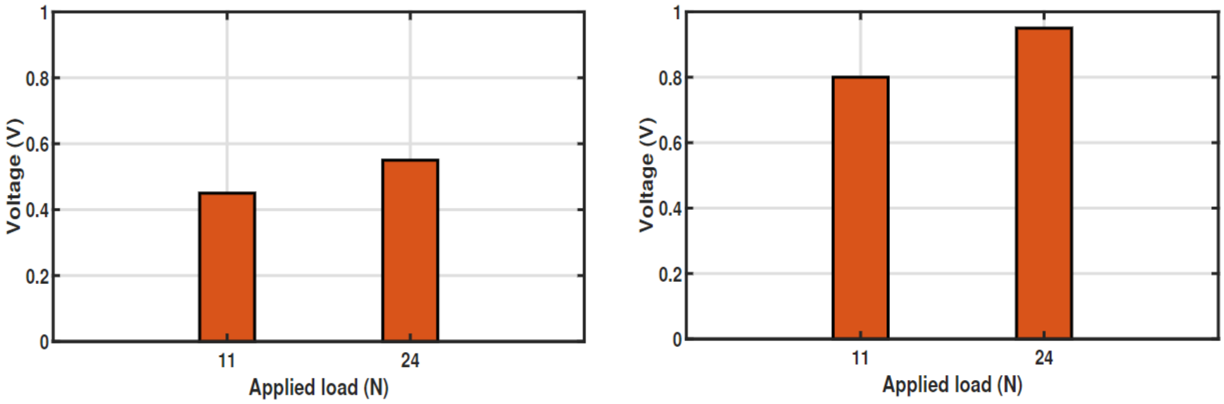

(a) **(b)**

Figure 4.5. Full knee harvester generated voltage amplitude bar plot loaded with 11 N and 24 N at: (a) 0.60 Hz, (b) 1.20 Hz.

Figure. 4.6 shows the outcomes of the triboelectric generator when changing the load frequency. The frequency of the gait cycle axial load exerted by the dynamic tester will be for low ranges, matching both senior and younger humans' walking activity. By holding the applied cyclic force at 11.0 N, the generated voltage signals for two different frequencies of 0.60 and 1.20 Hz are shown in Fig. 4.6a. The results show increasing output voltage with increasing the cyclic frequency. Also, by increasing the applied cyclic force to 24.0 N, the generated voltage signals for the two frequencies are shown in Fig. 4.6b, and higher amplitude voltage is observed. This increment is expected since higher frequency contributes to more contact and separation within a specific time, which means higher charge accumulation resulting in higher outputs. In Fig. 4.6, the voltage difference was calculated to be 0.15 V at both frequencies as shown in Fig. 4.6 a and b. This equality in the voltage difference is expected because the full knee configuration was tested under the same load and frequency conditions.

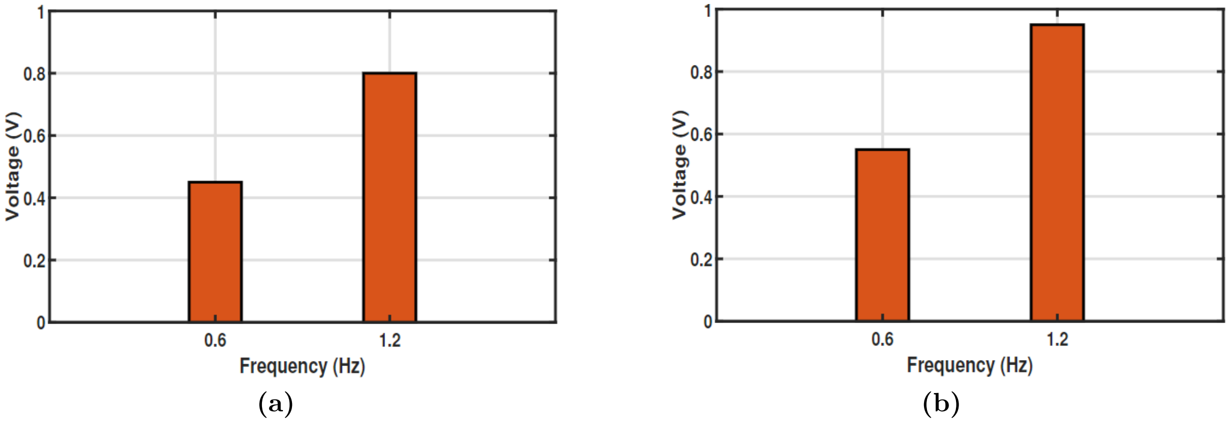

(a) (b)

Figure 4.6. Full knee harvester generated voltage amplitude bar plot at 0.6 Hz and 1.2 Hz frequencies, loaded at: (a) 11 N, (b) 24 N.

Lateral and Medial Configuration

The second harvester configuration with both lateral and medial parts was tested using the same loading and frequency conditions. The dynamic load at two different frequencies of 0.60 Hz and 1.20 Hz was applied to the harvester at a maximum of 11.0 N and 24.0 N. Because this harvester's configuration included two parts, results for each part were captured separately. For the lateral part with 11.0 N, the generated voltage at 0.60 Hz was equal to 0.20 V while at 1.20 Hz it was equal to 0.30 V as shown in Fig. 4.7a. Also, Fig. 4.7b shows the output from the medial position part of the harvester where 0.20 V were produced when the exerted force was at 0.60 Hz and changing the load frequency to 1.20 Hz caused the generated voltage to increase to 0.30 V. Both generators' results are equal because they are identical. Moreover, both figures show that the generated voltage is directly proportional to the load's frequency, similar to the full-knee harvester configuration findings.

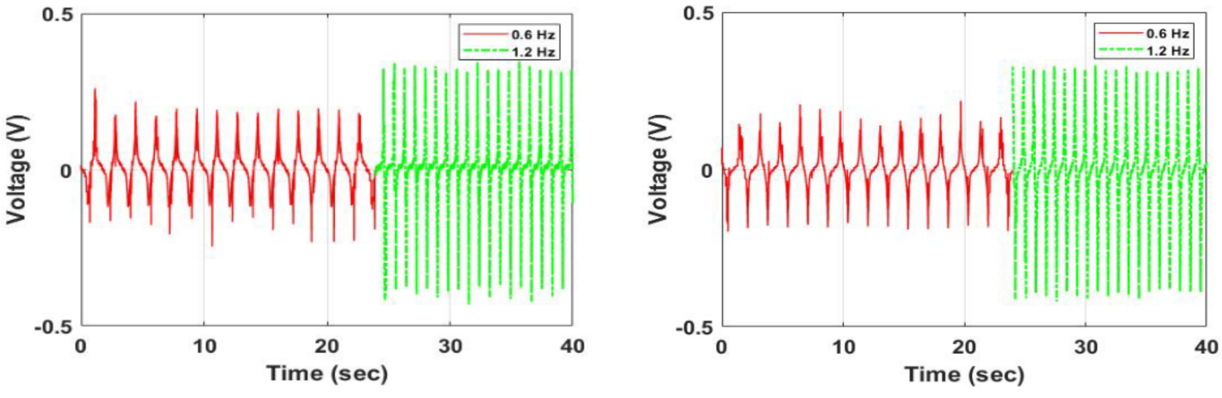

(a) (b)

Figure 4.7. Generated voltage at 0.6 Hz and 1.2 Hz at 11 N: (a) Lateral knee harvester (b) Medial knee harvester.

Since the accurate measurement of load imbalance can help to determine the wear in polyethylene, stress distribution in the implant and the implant-bone interface, and the stress transferred to the underlying bone [107], both lateral and medial harvesters were also tested with the maximum of 24 N at 0.60 Hz and 1.20 Hz. However, to match the actual load distribution in the knee under gait load, where the medial position shares more load than the lateral, the applied load is shifted toward the medial generator to create unbalance in the load distribution to be more focused on the medial position. Figure. 4.8 shows the output voltage with unbalanced 24.0 N for both lateral and medial positions. Compared to 11.0 N loading, it is clear that the voltage increased in the lateral location at 0.60 Hz and 1.20 Hz from 0.20 V to 0.40 V, and from 0.30 V to 0.50 V, respectively. For the medial position, the voltage increased remarkably to peak at 0.50 V and 0.80 V with the load of 24.0 N. This high increase in the medial part is expected because the load shifted to be more at this position, so a higher output voltage is expected to be produced. Figure. 4.9 shows how a load imbalance can be measured in the knee. In Fig. 4.9a, at 0.60 Hz and 1.20 Hz of loading with 11.0 N, the harvester at the medial position generates larger output voltages than the one at the lateral location but with a slight difference. These are identical triboelectric energy harvesters at both locations. When the load is increased to 24.0 N at either of the two testing frequencies of 0.60 Hz or 1.20 Hz, as shown in Fig. 4.9b, the difference in the generated voltage between the two parts increases remarkably. This indicates a load imbalance that the surgeon can use to reduce many of the complications after a total knee replacement as the surgeon can take action to fix problems such as misalignment, instability, and excessive wear.

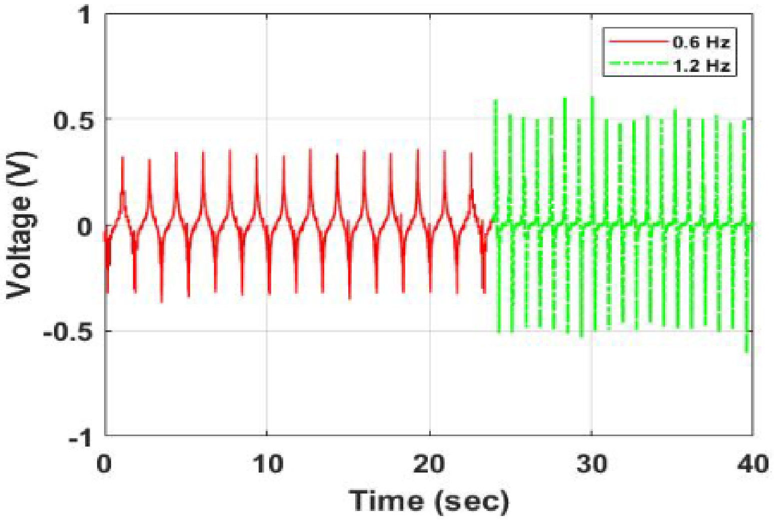

(a)

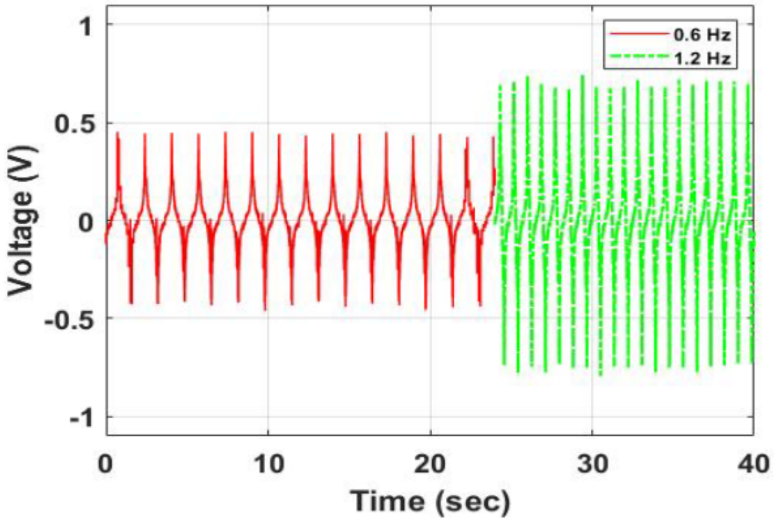

(b)

Figure 4.8. Generated voltage at 0.60 and 1.20 Hz: (a) Lateral knee harvester (b) Medial knee harvester, at 24.0 N.

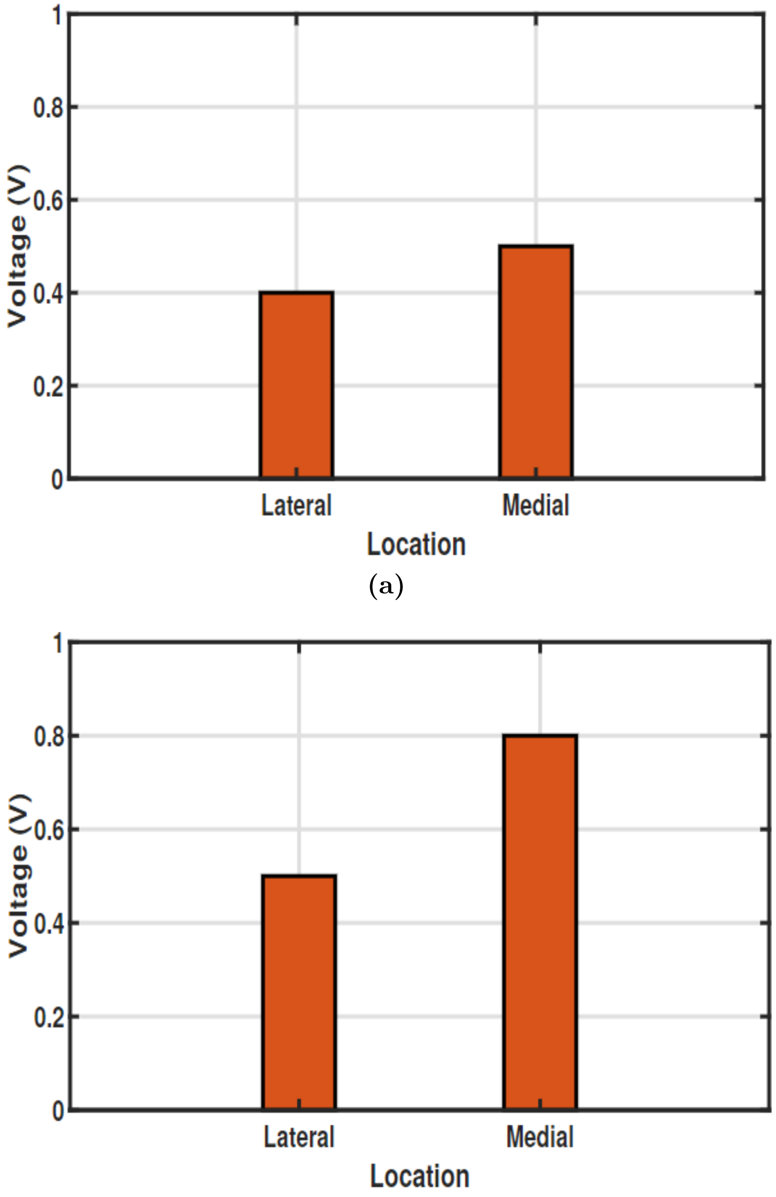

(a)

(b)

Figure 4.9. Lateral and Medial knee harvesters generated voltage amplitude bar plot at 24.0 N applied force: (a) 0.60 Hz, (b) 1.20 Hz.

Configurations comparison

Both configurations output voltage signals were rectified and compared at 1.20 Hz frequency and 24.0 N applied load as shown in Fig. 4.10. The Figure is divided into two plots: (a) Full knee harvester and (b) for the combined lateral and medial harvester. In Fig. 4.10a, the full harvester rectified generated voltage is accounted for nearly 0.90 V, while the lateral and medial harvester accounted for approximately 1.35 V as presented in Fig. 4.10b. This higher result at the lateral and medial together promises more efficient energy harvesting output by integrating two harvesters at both positions and the benefit of detecting the load imbalance in the knee.

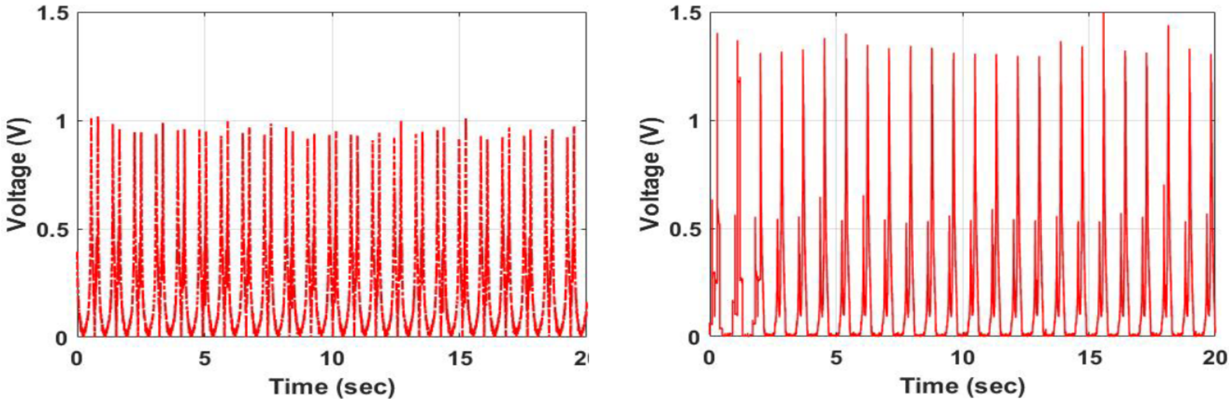

(a) **(b)**

Figure 4.10. Rectified generated voltage at 1.2Hz: (a) Lateral and Medial Assembly. (b) Full knee Assembly.

From all previous results before rectification, it is clearly shown that the full knee generator showed higher generated voltage at different frequencies compared to both lateral and medial positions under the same load. This investigation is related to the higher area of contact since the full configuration counts an area for 33.9 cm^2, while the area for each harvester at the lateral and medial positions is 12.9 cm^2. The rectified voltage for the combination of lateral and medial harvesters shows a higher output voltage than the full one. This finding would achieve more benefits in TKR since using harvesters at the lateral and medial positions is useful for the knee's load balance. Also, the generated voltage get is increasing by increasing the frequency. This can be related to the fact that higher frequencies correspond to more contact (more charges) between layers in a certain amount of time and thus higher power.

THR Load Monitoring System

Similar to the TKR, this section will focus on designing and retrofitting a Triboelectric energy harvester to THR. Hip implant geometry, manufacturing, and adapting the TEH to the hip geometry will be discussed as considerations in the design of the mechanical springs that will maintain the contact separation motion. The femoral head portion of the hip replacement will be designed to have microgrooves that follow approximately half of the sphere's diameter. Finite Element Analysis for the heme-spherical generator is carried out to find the optimal spring constant required to maintain the TEH's contact separation motion. The extracted parameters are implemented in a single-degree-of-freedom system with a piecewise function to model the contact and release modes and voltage estimations. The harvester can be adapted to the implant contour while optimizing energy and information collection transmitted to the medical person monitoring the implant's performance. This study will be considered the base for further investigation of triboelectric energy harvesting applications for load monitoring in total hip replacement.

Designing and Retrofitting a Triboelectric Energy Harvester to the THR

To be able to apply TEH designs to the hip replacement, a hip replacement must be modeled. SolidWorks was used to create all models. The hip replacement was designed within the ranges of different hip replacement sizes. A preliminary design was created to retrofit a TEH to the THR. A custom head was designed for total hip replacement. The custom head was designed to incorporate grooves onto the THR head, as shown in Fig. 4.11.

The triboelectric effect is caused by two materials of opposite tendency to gain or lose electrons coming in and out of contact. Thus, the surface area is a critical factor in the amount of energy produced. Creating grooves or ridges in mating surfaces increases the area of the surfaces in contact and consequently increases energy production [109–111]. Applying the same concept can maximize the energy generated from the triboelectric energy harvester in the hip implant, even without increasing the object's overall size. However, this can cause difficulty in manufacturing, especially during the prototype phases. The current design utilizes 300 μm tall grooves to increase surface area. However, the groove depth does not have to be this large during final production, so the groove size can be reduced to a much lower height to increase the contact area at the later production stage. Figure. 4.11, middle, shows various dimensions associated with the custom-designed femoral head. The spherical femoral head was designed with an outer diameter of 36 mm with the grooves extended only partly around the femoral head replacement due to the nature of the hip joint. The hip joint has a limited rotation angle; therefore, grooves extending 360 degrees are unnecessary. The grooves are rotated about the center axis with 20 degrees clockwise and 200 degrees counterclockwise, yielding a total usable TEH rotation of 220 degrees. The left side of Figure 4.11 demonstrates important overall dimensions of the femoral head.

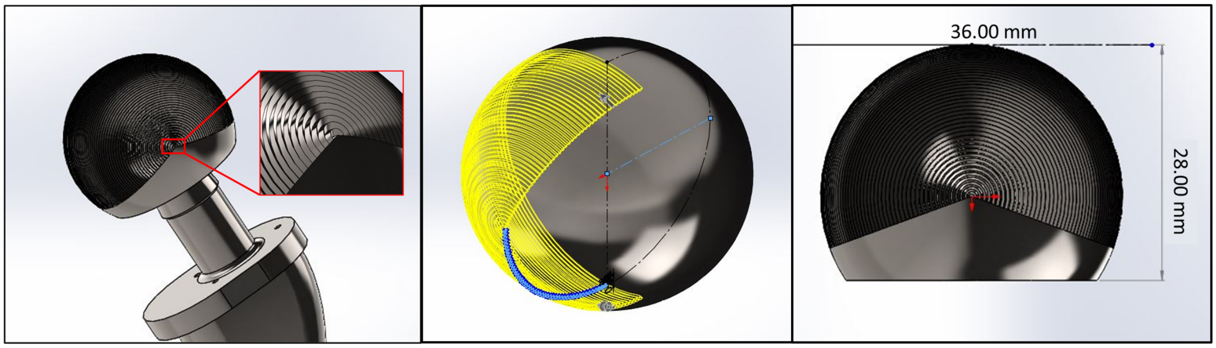

Figure 4.11. Custom designed femoral head attachment with grooves.

The THR retrofitted triboelectric energy harvester will resemble the 2D schematic flat surface shown in the left part of Figure 4.12. The TEH consists of two titanium layers and Polydimethylsiloxane (PDMS) insulator. These two materials have demonstrated successfully utilized in previous studies of applying a TEH to the total knee replacement (TKR), [92, 112, 113]. Titanium is used because of its superior interaction with biological environments, such as within the human body. The femoral head will act as the titanium layer, while the acetabular cup will serve as the opposite titanium layer. The acetabular cup is the socket that receives the femoral head. The cut-off parts in the hip implant generator point to the corresponding layers compared to a flat model shown in the middle schematic in Figure 4.12. The complete implanted generator attached to the pelvis is shown on the right side of Figure 4.12.

To further simplify the generator, a modified femoral head (femoral cup) was created as shown on the left side of Figure 4.13. This modified design will allow the FEA process for the mechanical springs discussed in the next section. Moreover, the right side of Figure 4.13 demonstrates the orientation of the mating grooves when all three pieces are placed together to create the whole TEH. The gap between the PDMS grooves and the femoral head grooves is considered to be 100 μm. The total PDMS height is 500 μm with 300 μm for the ridge height and 200 μm for the base height.

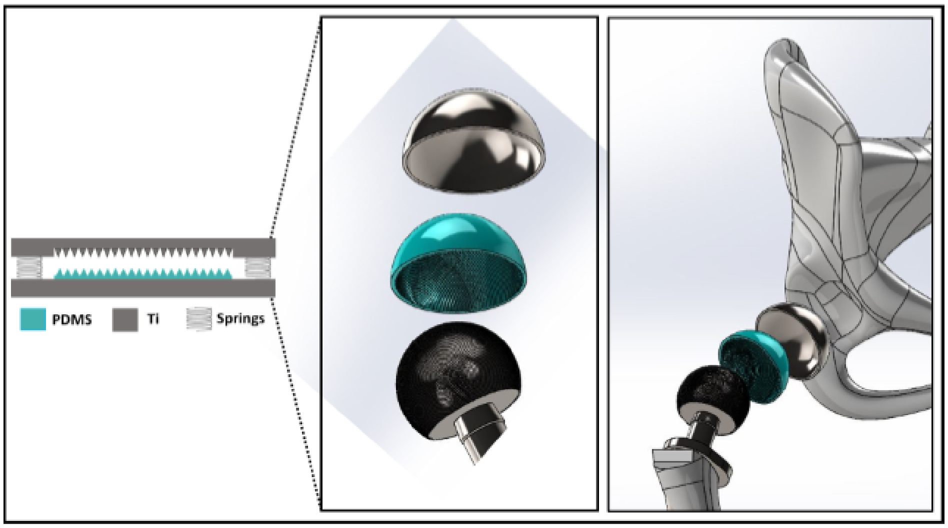

Figure 4.12. TEH layers and comparison to a flat model.

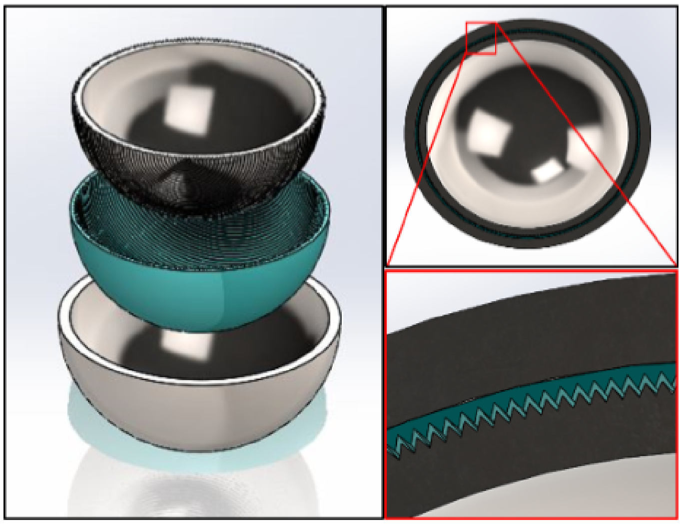

Figure 4.13. Modified Femoral Cup Design.

Springs Design Using Finite Element Analysis of the TEH

Since triboelectric energy harvesters rely on materials properties and geometry that will be coming in and out of contact, the current design shown in Figure 4.13 will only work if the materials come out of contact after experiencing force to come in contact. Therefore, Titanium cantilever springs will be used to return the femoral cup to its original, uncompressed position. Different concepts can be suggested for this mechanism. The first concept is based on a cantilever spring design idea as shown in Figure 4.14. This concept consists of 16 pins uniformly distributed on the generator edge, holding the edges together at a relatively constant location. Each pin is attached to both outer and inner femoral cups and acts as a mechanical spring that will return the two femoral cups to their original relative location after getting displaced by force. In other words, the pins maintain the contact and separation motion in the TEH.

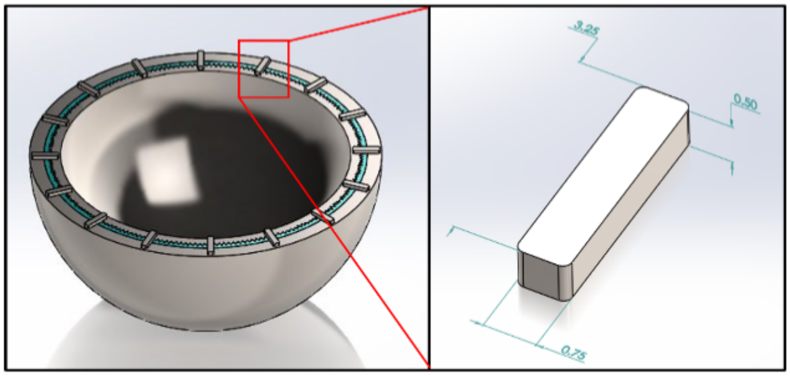

Figure 4.14. Triboelectric Energy Harvester with Cantilever Springs and their dimensions.

An initial investigation for the displacement for the design shown in Figure 4.14 was performed by FEA with the applied load of 2500 N, and the load is assumed to be distributed equally by all the nodes associated with the generator. The lower electrode is considered fixed, and the load is applied in the vertical direction. The material utilized in this analysis consists of a linear elastic, isotropic material. Model loading consists of the applied mechanical load, modeled as the load control and the displacement control. The outer sides of the springs are attached to the outer femoral cup and are ideally assumed to have zero displacements. On the other hand, the inner side of the springs attached to the inner femoral cup will move under the applied load for contact and separation. Figure 4.15 shows that the maximum linear displacement with the magnitude of (241 μm) at 2500 N applied load will contact partially with the PDMS the surface area of contact is small. Therefore the expected output voltage will be small. However, the manufacturing and repair are still a challenge for this design since cantilever springs mounted on the top of the cups need to be either welded or attached with micro-screws to secure the fit. Moreover, the pins have rounded edges that require specific machines with high precision, leading to a high manufacturing cost due to the required accuracy.

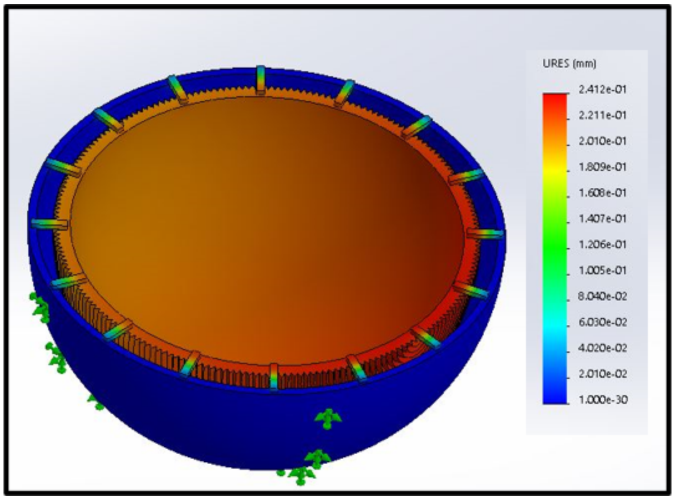

Figure 4.15. Von Mises and Displacement FEA results for the Triboelectric Energy Harvester Cantilever Springs.

However, to tackle the previous design challenges, a new optimized design with new geometry is proposed, as shown in Figure 4.16. The new pins' geometry has better functionality since those pins penetrate the whole layers of the assembly, the femoral head, PDMS, and acetabular cup, as shown in the middle of Figure 4.16. Besides, the number of pins has been reduced to increase the linear displacement that would be achieved for full engagement between the femoral head and PDMS for a higher area of contact translated into a higher voltage. In the middle of Figure 4.16, the femoral cup, acetabular cup, and PDMS layer were made transparent to recognize the location and penetration of the pins better. The new pin design incorporates only four titanium pins spaced 90 degrees apart. The pins' dimensions were obtained through FEA analysis using a SolidWorks static simulation model, which was performed to demonstrate the viability of the Titanium mechanical pin springs and their properties. A static simulation model is used when objects at rest experience forces. However, to carry out the new design's FEA, the acetabular cup was assumed to be fixed and will not have to be displaced by any affecting force. Moreover, the applied force on the femoral cup is assumed to be uniformly distributed over the surface and applied in the vertical direction in a quasi-static process. The dimensions of the new design pins are shown in the right of Figure 4.16. The new design was tested at a quasi-statically applied load that gradually increased while monitoring the linear displacement of the springs to determine the load associated with the maximum allowable linear displacement of 600 μm.

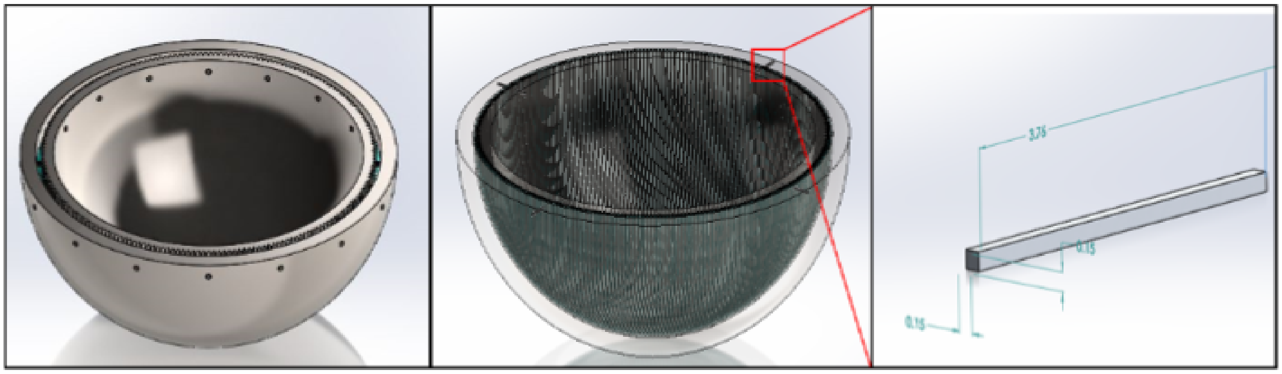

Figure 4.16. Updated cantilever spring design with the new dimensions.

The new design was tested by FEA under a range of loads to get the optimum applied load corresponding to the maximum allowable linear displacement, which is 600 μm, and to get the new springs' stiffness to serve properly under the loading conditions. Figure 4.17

shows the simulated linear displacement of the springs under a range of forces. From the Figure, the femoral head will come in contact with the PDMS layer under an applied load between $300 - 350$ N. This is a viable relationship because the hip joint under little load shows forces of approximately 500 N [97]. According to the data shown in Figure 4.17, the load corresponding to the maximum possible linear displacement of 600 μm was found to be 1850 N, which is much less than 2500 N but still maintains the required contact-separation motion. Accordingly, a superior representation of the pins' material properties is represented by calculating the spring constant (k) associated with the cantilever spring pins. Hooke's law can be used to calculate the spring constant of a cantilever with a rectangular cross-section (k = F/x), where F is the force applied in Newtons, and x is the displacement in one axis which is, in this case, the y-axis. According to Hooke's law, the spring constant represents the slope of the line shown in Figure 4.17, which is equal to 3072 N/mm. This value is considered the desired material stiffness used for the pins in triboelectric energy harvester design.

Figure 4.18 shows the simulated surface area of contact between the upper femoral cup (upper electrode) and the PDMS layer under an applied force. No contact occurs when the applied force between the upper electrode and the PDMS layer is below 309 N. When the applied force value goes above 309 N and up to 1230 N, the surface area of contact act linearly. Beyond the 1230 N, the contact surface area reaches a maximum possible value of $82 * 10^{-}6$ m^2, even at higher applied loads.

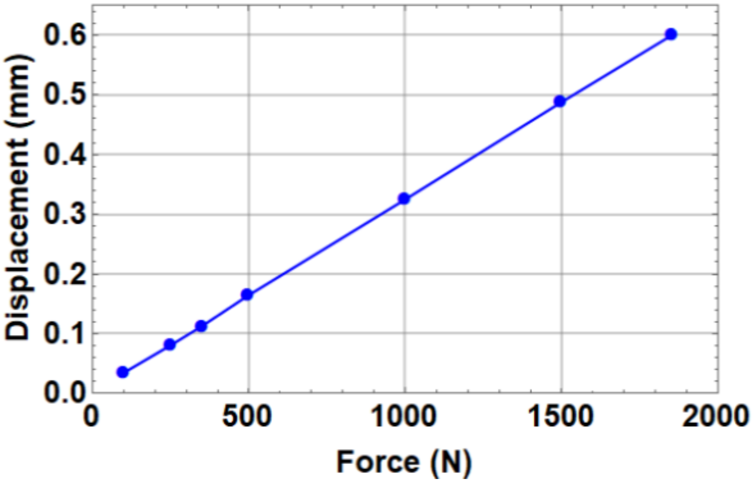

Figure 4.17. Displacement of the femoral cup resulting from applying force resisted by the pin springs.

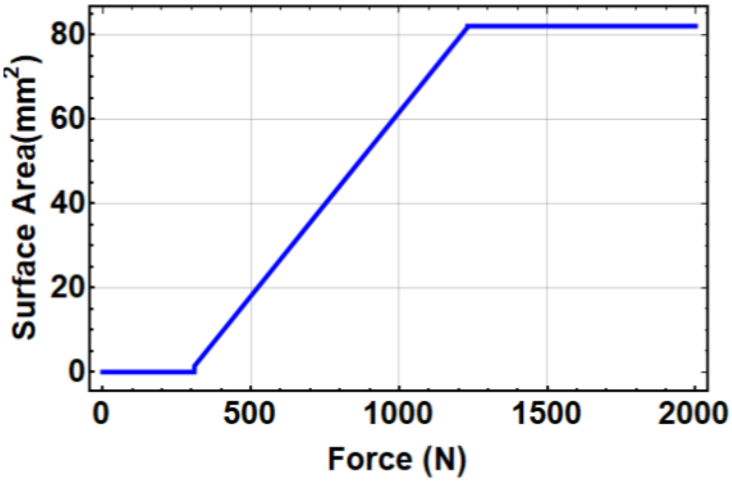

Figure 4.18. Surface area of contact vs. applied force.

Mathematical Model

The FEA results were implemented in a single-degree-of-freedom system with a piecewise function to model the contact and release modes and estimate produced voltage. According to Figure 4.17, the upper femoral cup will start to displace at a minimum force of 100 N and reach the maximum displacement of 0.6 mm at 1850 N. Accordingly, the displacement of the springs will increase proportionally to the increased applied force. As a result, the upper femoral cup will undergo a half-sine wave which can be represented mathematically by the following piecewise form:

$$y(t) = \begin{cases} Y_0 Sin(2\pi\Omega t), & y(t) \leq 0 \\ 0, & y(t) > 0 \end{cases} \tag{4.1}$$

Where Ω is the frequency of motion considered 1 Hz matching regular human walking motion. Y_0 is the amplitude of the displacement, which is a function of the applied force (F) as shown in Figure 4.17. Mathematically, it is given by the following equation:

$$Y_0 = 3.26 * 10^{-10} * F \tag{4.2}$$

In a similar way and according to the result obtained in Figure 4.18, the surface area of contact between the upper electrode and the PDMS layer can also be calculated as a function of the applied force and can be modeled using a piecewise function in the following form:

$$S(F) = \begin{cases} 0, & 0 \leq F < 309.4 \\ 82 * 10^{-6} * \left(\frac{F-293.26}{940.46}\right), & 309.4 \leq F < 1230.06 \\ 82 * 10^{-6}, & F \geq 1230.06 \end{cases} \tag{4.3}$$

The mechanical springs will hold the upper femoral cup, which acts as an upper electrode. The upper electrode will be displaced toward the PDMS layer when the system undergoes a vertical load. When the applied load is removed, the springs return the upper electrode to its original position. When the applied load becomes cyclic, a contact and separation motion between the two layers will be created, and a charge electrification generation will occur. The upper and lower electrodes of the THR triboelectric generator are simplified to act as a parallel plate capacitor. As a result, two electrical fields are generated, one at the PDMS layer and one at the air gap between the two electrodes. According to this, the electrical equation that governs the output voltage is given by:

$$\dot{q}(t) = -\frac{q(t)}{R\epsilon_0 S_{max}}\left(\frac{T}{\epsilon_r} - y(t)\right) + \frac{\sigma S(F)}{R\epsilon_0 S_{max}} y(t) \tag{4.4}$$

Where $q(t)$ is the number of transferred charges between the two electrodes, S_{max} is the maximum area of contact extracted from the FEA results and equal to $82 * 10^{-}6$ m^2. R is the resistance, and T is the thickness of the PDMS layer. $\epsilon_0 = 8.85 * 10^{-12}$ F/m is the vacuum permittivity, ϵ_r is the dielectric constant of the PDMS, and σ is the surface charge density.

The surface charge density is a function of multiple factors, such as the materials' chemical properties and the micro-surface patterns that control the area of contact [114]. Therefore, to counter this variability in the model, the surface charge density is assumed to be a function of the ratio between the surface area at any force and the maximum area of contact shown by equation 5, which is proportional to the force applied.

$$\sigma(F) = 80 * 10^{-6} \left(\frac{S(F)}{S_{max}} \right) \tag{4.5}$$

Table 4.1. Parameters used in the model.

Parameters		**Value**
Forcing Frequency	Ω	$1\ Hz$
PDMS Thickness	T	$500\ \mu m$
Permeability of free space	ϵ_0	$8.85 * 10^{-12}\ F/m$
Permeability of PDMS	ϵ_r	$3.4\ F/m$
Resistance	R	$10\ M\Omega$

The voltage produced by the generator is the total voltage produced in the air gap and the

PDMS layer. By solving equations 1-5 using the parameters on Table. 4.1, we can estimate the voltage signal produced at any applied force. Figure 4.19a shows the displacement profile resulting from applying 1000 N cyclic loads. The maximum displacement reached is around 0.3 mm, which matches the results from Figure 4.17. The corresponding generated voltage signal is shown in Figure 4.19b, where the maximum output voltage of 10 V is generated.

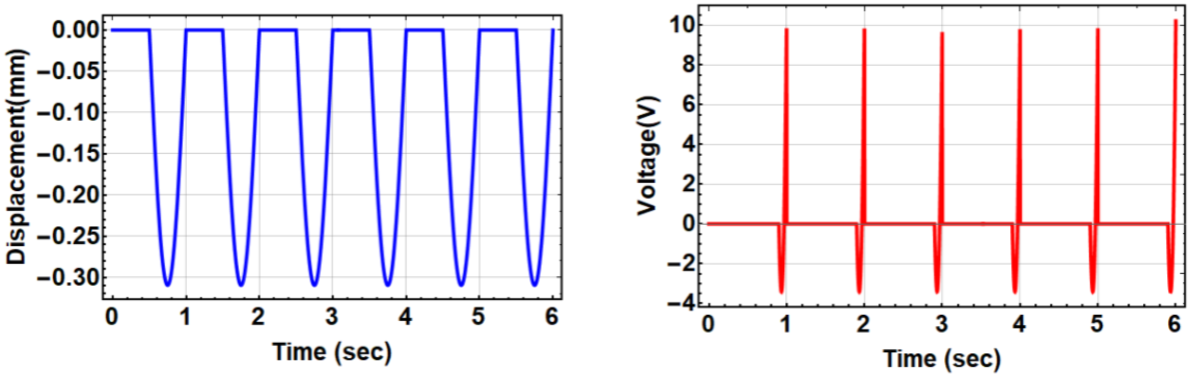

(a)

(b)

Figure 4.19. Simulated results of an applied load of 1000 N: (a) Displacement vs. time response, (b) Simulated voltage output from the THR triboelectric generator.

Increasing the applied load amplitude to 1500 N results in a higher displacement amplitude of 0.48 mm, as shown in Figure 4.20a. This increment in the applied load results in a significant increase in the generated voltage signal shown in Figure 4.20b, where the maximum output voltage reaches 15 V.

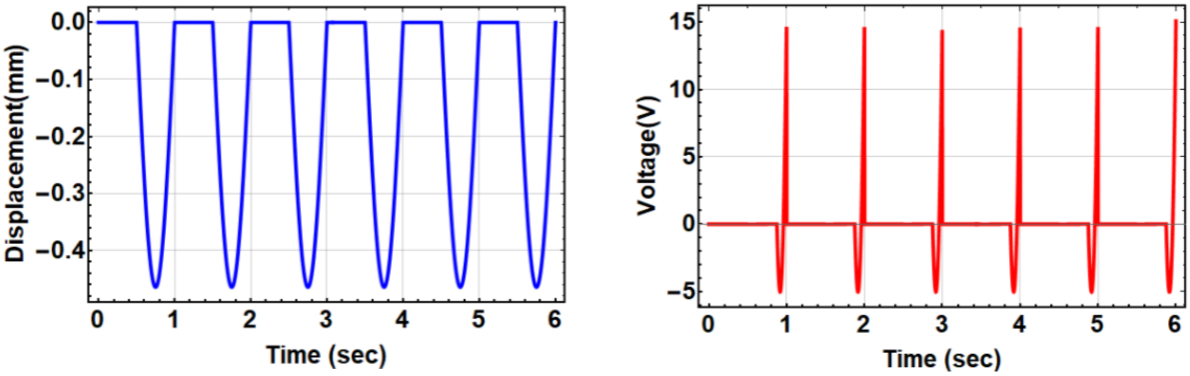

(a) **(b)**

Figure 4.20. Simulated results at an applied load of 1500 N: (a) Displacement vs. time response, (b) Simulated voltage output from the THR triboelectric generator.

Chapter Five

Conclusion and Summary

In summary, a vibration-based piezoelectric energy harvester using a mechanical frequency up-conversion method for low-frequency vibrations is presented. The proposed structure consists of a low-frequency beam (LFB) made of soft polymer for low natural frequency and a high-frequency bimorph beam (HFB) made of Aluminum with piezoelectric layers for high natural frequency, and both have identical tip magnets facing each other with the same polarity, as proposed in the first modeling and simulation analysis. Two Degree of Freedom (2DOF) lumped parameter model to study the static and dynamic behavior of the system has been developed. The frequency up-converter converts low-frequency vibrations to a higher frequency, which is the resonance frequency of the LFB. The static analysis for the harvester revealed a 15 mm threshold distance that divided the harvester response into monostable ($d > d_{th}$) and bistable ($d < d_{th}$) regimes based on the distance between two magnets. Under no magnetic effect, natural frequencies of 24 Hz and 256 Hz are reported for LFB and HFB, respectively. Under the light magnetic influence, a generated voltage waveform presented at 24 Hz, proving the frequency up-conversion. Increasing the magnetic coupling by lowering the distance between the two magnets to the threshold and bistable regions results in shifting the frequency to 18.5 Hz and 41 Hz, respectively. Besides, increasing the excitation level revealed nonlinear phenomena of hardening and softening behaviors at the threshold and the bistable regions, respectively. Also, at 1.5 g excitation level, the voltage generated at the bistable region increment 500 % and 192% compared to the monostable and the threshold regions. This shows the feasibility of the proposed frequency up-converter in powerless microsystem applications operating at low-frequency vibration mediums.

In the frequency up-converter experimental validation, the HFB has been changed to be a unimorph HFB, which means only a single piezoelectric layer is attached to the beam. Also, the physical dimensions of the LFB and HFB have been changed. The investigation started with the static analysis that resulted in a $15mm$ separation distance as a critical distance that divides the system into monostable and bistable regions, where at $d > d_{th}$ is the monostable region and at $d < d_{th}$ is the bistable region. The linear response of the system where the effect of the magnetic nonlinearity is eliminated ($F_{magy} = 0$) is elevated that the natural frequency of the LFB is $21Hz$ and $263Hz$ for the HFB. At the monostable region ($d = 35mm$), a nonlinear hardening behavior was captured with increasing the excitation level. Also, a voltage signal is generated with the magnitude of $1mV$ at $21Hz$, which is the natural frequency of the LFB, and this proves the frequency up-conversion concept. At the threshold ($d = 15mm$), a softening behavior showed up when the natural frequency dropped to $17Hz$ at $0.1g$ excitation level compared to the linear natural frequency that equals $20.8Hz$. This shift is due to the dominance of the quadratic nonlinearity at low excitation levels at this distance. Increasing the excitation level at the same distance resulted in a combination of nonlinear softening and hardening behavior where the system switched its behavior from softening to hardening after $0.5g$ excitation level. This behavior switches because the quadratic nonlinearity becomes dominant at higher excitation levels. By decreasing the separation distance to reach the bistable region at $d = 8mm$, where the magnetic force is stronger, the generated voltage peaked at $30Hz$, and this shift of the natural frequency indicates a hardening behavior compared to the linear natural frequency of $20.8Hz$ at $0.1g$ excitation level. The natural frequency increases due to the dominance of the cubic nonlinearity, while the quadratic nonlinearity dominates at higher excitation levels, so a softening behavior occurs. By decreasing the separation distance to $d = 5mm$, the natural frequency increased to $37.2Hz$, which is a hardening behavior. The softening behavior is noticed at higher excitation levels, duo to the cubic and quadratic nonlinearity dominance, respectively. For the bistable at $0.1g$ excitation level, the generated voltage increased by 1000% by recording $10mV$ in the bistable at $d = 8mm$ and 4000% at $d = 5mm$ compared to $1mV$ in the monostable at the same excitation level. In addition, a $25M\Omega$

external resistance was found to be the maximum value where the generated voltage in the system maximized at approximately $2V$.

Triboelectric energy harvesters for TKR load sensing applications have been investigated. Two different configurations were tested under cycling load using a dynamic tester. It has been found that the generated voltage increases with increasing the frequency for both configurations. Moreover, using a full knee harvester would produce more voltage than both harvesters at lateral and medial positions since the results show that the output voltage is proportional to the contact area. For the lateral and medial configuration, it was found that when the load is applied to the center position, the medial position has almost the same generated voltage compared to the lateral position. While applying the load with some shifting toward the medial location, to create an imbalance situation, the generator at the medial location shows higher amplitude than the lateral generator, which indicates the imbalance detection possibility. This result promises to use these harvesters to measure the knee load distribution after TKR, allowing implant imbalance detection to prevent postoperative problems such as implant wear and function loosening. Furthermore, the results showed that the rectified output voltage for combined lateral and medial harvesters produces more output voltage than the full configurations. This is an additive value to the load imbalance measurement for both lateral and medial. The triboelectric transduction mechanism is a promising concept with the potential to provide long-term feedback in implanted TKR.

In addition, a novel design of Triboelectric Energy Harvester (TEH) for retrofitting into a THR implant was proposed upgrading THRs to a smart implant. The proposed design incorporates grooves onto the THR femoral head to maximize energy production without any significant femoral head size change. Design iterations of a mechanism to maintain the contact-separation motion of the TEH were carried out using FEA. The mechanism consisted of strategically distributed solid pin springs. The walking profile was simulated by a half-sine wave function applied to the proposed design to extract the spring stiffness and the relation between the TEH and the applied force's displacement. This relation was extended to a single-degree-of-freedom model of the TEH parts displacement and surface area of contact as functions of the load transferred to the hip implant. The model was augmented by implementing results from the FEA and utilizing piecewise functions to estimate produced voltage as a function of the contact and release modes. The model shows a proportional relationship between the produced voltage and the applied load. This analysis is considered a feasibility study for new research in load monitoring for total hip replacement.

References

[1] A. Erturk, “Piezoelectric energy harvesting for civil infrastructure system applications: Moving loads and surface strain fluctuations,” *Journal of Intelligent Material systems and structures*, vol. 22, no. 17, pp. 1959–1973, 2011.

[2] A. Wickenheiser and E. Garcia, “Broadband vibration-based energy harvesting improvement through frequency up-conversion by magnetic excitation,” *Smart Materials and Structures*, vol. 19, no. 6, p. 065020, 2010.

[3] J. Noh, P. Kim, and Y.-J. Yoon, “Load resistance optimization of a magnetically coupled two-degree-of-freedom bistable energy harvester considering third-harmonic distortion in forced oscillation,” *Sensors*, vol. 21, no. 8, p. 2668, 2021.

[4] M. Safaei, R. M. Meneghini, and S. R. Anton, “Energy harvesting and sensing with embedded piezoelectric ceramics in knee implants,” *IEEE/ASME Transactions on Mechatronics*, 2018.

[5] A. Ibrahim, G. Yamomo, R. Willing, and S. Towfighian, “Parametric study of a triboelectric transducer in total knee replacement application,” *Intelligent Material*

Systems and Structures, 2020.

[6] J. Sullivan, L. Gaines, *et al.*, “A review of battery life-cycle analysis: state of knowledge and critical needs.,” 2010.

[7] S. Roundy, P. K. Wright, and J. Rabaey, “A study of low level vibrations as a power source for wireless sensor nodes,” *Computer communications*, vol. 26, no. 11, pp. 1131–1144, 2003.

[8] L. M. Miller, E. Halvorsen, T. Dong, and P. K. Wright, “Modeling and experimental verification of low-frequency mems energy harvesting from ambient vibrations,” *Journal of Micromechanics and Microengineering*, vol. 21, no. 4, p. 045029, 2011.

[9] D. Paci, M. Schipani, V. Bottarel, and D. Miatton, “Optimization of a piezoelectric energy harvester for environmental broadband vibrations,” in *2008 15th IEEE International Conference on Electronics, Circuits and Systems*, pp. 177–181, IEEE, 2008.

[10] A. Ibrahim, S. Towfighian, M. Younis, and Q. Su, “Magnetoelastic beam with extended polymer for low frequency vibration energy harvesting,” in *SPIE Smart Structures and Materials+ Nondestructive Evaluation and Health Monitoring*, pp. 98060B–98060B, International Society for Optics and Photonics, 2016.

[11] S. R. McNutt, “Observations and analysis of b-type earthquakes, explosions, and volcanic tremor at pavlof volcano, alaska,” *Bulletin of the Seismological Society of America*, vol. 76, no. 1, pp. 153–175, 1986.

[12] E. K. Reilly, L. M. Miller, R. Fain, and P. Wright, “A study of ambient vibrations for piezoelectric energy conversion,” *Proc. PowerMEMS*, vol. 2009, pp. 312–315, 2009.

[13] Y. Tan, Y. Dong, and X. Wang, “Review of mems electromagnetic vibration energy harvester,” *Journal of Microelectromechanical Systems*, vol. 26, no. 1, pp. 1–16, 2016.

[14] C. Zhao, Y. Yang, D. Upadrashta, and L. Zhao, “Design, modeling and experimental validation of a low-frequency cantilever triboelectric energy harvester,” *Energy*, vol. 214, p. 118885, 2021.

[15] A. Ibrahim, A. Ramini, and S. Towfighian, “Triboelectric energy harvester with large bandwidth under harmonic and random excitations,” *Energy Reports*, vol. 6, pp. 2490–2502, 2020.

[16] H. S. Kim, J.-H. Kim, and J. Kim, “A review of piezoelectric energy harvesting based on vibration,” *International journal of precision engineering and manufacturing*, vol. 12, no. 6, pp. 1129–1141, 2011.

[17] M. Amin Karami and D. J. Inman, “Powering pacemakers from heartbeat vibrations using linear and nonlinear energy harvesters,” *Applied Physics Letters*, vol. 100, no. 4, p. 042901, 2012.

[18] Y. Qi, N. T. Jafferis, K. Lyons Jr, C. M. Lee, H. Ahmad, and M. C. McAlpine, “Piezoelectric ribbons printed onto rubber for flexible energy conversion,” *Nano letters*, vol. 10, no. 2, pp. 524–528, 2010.

[19] S. Ali, S. Adhikari, M. Friswell, and S. Narayanan, “The analysis of piezomagnetoelastic energy harvesters under broadband random excitations,” *Journal of Applied Physics*, vol. 109, no. 7, p. 074904, 2011.

[20] S. R. Anton, A. Erturk, and D. J. Inman, “Multifunctional unmanned aerial vehicle wing spar for low-power generation and storage,” *Journal of Aircraft*, vol. 49, no. 1, pp. 292–301, 2012.

[21] A. Erturk, J. M. Renno, and D. J. Inman, “Modeling of piezoelectric energy harvesting from an l-shaped beam-mass structure with an application to uavs,” *Journal of intelligent material systems and structures*, vol. 20, no. 5, pp. 529–544, 2009.

[22] C. A. Featherston, K. M. Holford, and B. Greaves, “Harvesting vibration energy for structural health monitoring in aircraft,” in *Key Engineering Materials*, vol. 413, pp. 439–446, Trans Tech Publ, 2009.

[23] S. Lee and B. D. Youn, "A new piezoelectric energy harvesting design concept: multimodal energy harvesting skin," *IEEE transactions on ultrasonics, ferroelectrics, and frequency control*, vol. 58, no. 3, pp. 629–645, 2011.

[24] M. Q. Le, J.-F. Capsal, M. Lallart, Y. Hebrard, A. Van Der Ham, N. Reffe, L. Geynet, and P.-J. Cottinet, "Review on energy harvesting for structural health monitoring in aeronautical applications," *Progress in Aerospace Sciences*, vol. 79, pp. 147–157, 2015.

[25] B. Mann and N. Sims, "Energy harvesting from the nonlinear oscillations of magnetic levitation," *Journal of Sound and Vibration*, vol. 319, no. 1, pp. 515–530, 2009.

[26] A. Erturk and D. Inman, "Broadband piezoelectric power generation on high-energy orbits of the bistable duffing oscillator with electromechanical coupling," *Journal of Sound and Vibration*, vol. 330, no. 10, pp. 2339–2353, 2011.

[27] A. Triplett and D. D. Quinn, "The effect of non-linear piezoelectric coupling on vibration-based energy harvesting," *Journal of Intelligent Material Systems and Structures*, vol. 20, no. 16, pp. 1959–1967, 2009.

[28] S. C. Stanton, C. C. McGehee, and B. P. Mann, "Nonlinear dynamics for broadband energy harvesting: investigation of a bistable piezoelectric inertial generator," *Physica D: Nonlinear Phenomena*, vol. 239, no. 10, pp. 640–653, 2010.

[29] P. Kim, S. Bae, and J. Seok, “Resonant behaviors of a nonlinear cantilever beam with tip mass subject to an axial force and electrostatic excitation,” *International Journal of Mechanical Sciences*, vol. 64, no. 1, pp. 232–257, 2012.

[30] A. Abdelkefi, A. Nayfeh, and M. Hajj, “Global nonlinear distributed-parameter model of parametrically excited piezoelectric energy harvesters,” *Nonlinear Dynamics*, vol. 67, no. 2, pp. 1147–1160, 2012.

[31] P. Kim, Y.-J. Yoon, and J. Seok, “Nonlinear dynamic analyses on a magnetopiezoelastic energy harvester with reversible hysteresis,” *Nonlinear Dynamics*, vol. 83, no. 4, pp. 1823–1854, 2016.

[32] M. P. S. Dos Santos, J. A. Ferreira, J. A. Simões, R. Pascoal, J. Torrão, X. Xue, and E. P. Furlani, “Magnetic levitation-based electromagnetic energy harvesting: a semi-analytical non-linear model for energy transduction,” *Scientific reports*, vol. 6, no. 1, pp. 1–9, 2016.

[33] M.-L. Seol, J.-W. Han, S.-B. Jeon, M. Meyyappan, and Y.-K. Choi, “Floating oscillator-embedded triboelectric generator for versatile mechanical energy harvesting,” *Scientific reports*, vol. 5, no. 1, pp. 1–10, 2015.

[34] A. Ibrahim, S. Towfighian, and M. I. Younis, “Dynamics of transition regime in bistable vibration energy harvesters,” *Journal of Vibration and Acoustics*, vol. 139, no. 5, p. 051008, 2017.

[35] C. Covaci and A. Gontean, “Piezoelectric energy harvesting solutions: A review,” *Sensors*, vol. 20, no. 12, p. 3512, 2020.

[36] I. Izadgoshasb, Y. Y. Lim, L. Tang, R. V. Padilla, Z. S. Tang, and M. Sedighi, “Improving efficiency of piezoelectric based energy harvesting from human motions using double pendulum system,” *Energy Conversion and Management*, vol. 184, pp. 559–570, 2019.

[37] S. W. Ibrahim and W. G. Ali, “A review on frequency tuning methods for piezoelectric energy harvesting systems,” *Journal of renewable and sustainable energy*, vol. 4, no. 6, p. 062703, 2012.

[38] D. Zhu, S. Roberts, M. J. Tudor, and S. P. Beeby, “Design and experimental characterization of a tunable vibration-based electromagnetic micro-generator,” *Sensors and Actuators A: Physical*, vol. 158, no. 2, pp. 284–293, 2010.

[39] W. Sun, J. Jung, X. Y. Wang, P. Kim, J. Seok, and D.-y. Jang, “Design, simulation, and optimization of a frequency-tunable vibration energy harvester that uses a

magnetorheological elastomer," *Advances in Mechanical Engineering*, vol. 7, no. 1, p. 147421, 2015.

[40] L. Gammaitoni, I. Neri, and H. Vocca, "Nonlinear oscillators for vibration energy harvesting," *Applied Physics Letters*, vol. 94, no. 16, p. 164102, 2009.

[41] R. Masana and M. F. Daqaq, "Electromechanical modeling and nonlinear analysis of axially loaded energy harvesters," *Journal of Vibration and Acoustics*, vol. 133, no. 1, p. 011007, 2011.

[42] M. S. Soliman, E. M. Abdel-Rahman, E. F. El-Saadany, and R. R. Mansour, "A design procedure for wideband micropower generators," *Journal of Microelectromechanical Systems*, vol. 18, no. 6, pp. 1288–1299, 2009.

[43] F. Moon and P. J. Holmes, "A magnetoelastic strange attractor," *Journal of Sound and Vibration*, vol. 65, no. 2, pp. 275–296, 1979.

[44] S. C. Stanton, B. A. Owens, and B. P. Mann, "Harmonic balance analysis of the bistable piezoelectric inertial generator," *Journal of Sound and Vibration*, vol. 331, no. 15, pp. 3617–3627, 2012.

[45] L. Gu and C. Livermore, "Impact-driven, frequency up-converting coupled vibration energy harvesting device for low frequency operation," *Smart Materials and Structures*, vol. 20, no. 4, p. 045004, 2011.

[46] H. Liu, C. Lee, T. Kobayashi, C. J. Tay, and C. Quan, "Piezoelectric mems-based wideband energy harvesting systems using a frequency-up-conversion cantilever stopper," *Sensors and Actuators A: Physical*, vol. 186, pp. 242–248, 2012.

[47] Ö. Zorlu, E. T. Topal, and H. Külah, "A vibration-based electromagnetic energy harvester using mechanical frequency up-conversion method," *IEEE Sensors Journal*, vol. 11, no. 2, pp. 481–488, 2010.

[48] I. Sari, T. Balkan, and H. Külah, "An electromagnetic micro power generator for low-frequency environmental vibrations based on the frequency upconversion technique," *Journal of Microelectromechanical systems*, vol. 19, no. 1, pp. 14–27, 2009.

[49] T. Galchev, H. Kim, and K. Najafi, "Micro power generator for harvesting low-frequency and nonperiodic vibrations," *Journal of Microelectromechanical Systems*, vol. 20, no. 4, pp. 852–866, 2011.

[50] K. Ashraf, M. M. Khir, J. Dennis, and Z. Baharudin, "A wideband, frequency up-converting bounded vibration energy harvester for a low-frequency environment," *Smart materials and structures*, vol. 22, no. 2, p. 025018, 2013.

[51] E. Fakeih, *Harvesting Mechanical Vibrations using a Frequency Up-converter.* PhD thesis, 2020.

[52] E. Fakeih, A. S. Almansouri, J. Kosel, M. I. Younis, and K. N. Salama, "A wideband magnetic frequency up-converter energy harvester," *Advanced Engineering Materials*, p. 2001364, 2021.

[53] M. Atmeh and A. Ibrahim, "Modeling of piezoelectric vibration energy harvesting from low-frequency using frequency up-conversion," in *Smart Materials, Adaptive Structures and Intelligent Systems*, vol. 85499, p. V001T04A011, American Society of Mechanical Engineers, 2021.

[54] B. Edwards, M. Xie, K. Aw, A. Hu, and W. Gao, "An impact based frequency up-conversion mechanism for low frequency vibration energy harvesting," in *2013 Transducers & Eurosensors XXVII: The 17th International Conference on Solid-State Sensors, Actuators and Microsystems (TRANSDUCERS & EUROSENSORS XXVII)*, pp. 1344–1347, IEEE, 2013.

[55] H. Liu, C. Lee, T. Kobayashi, C. J. Tay, and C. Quan, "Investigation of a mems piezoelectric energy harvester system with a frequency-widened-bandwidth mechanism introduced by mechanical stoppers," *Smart Materials and Structures*, vol. 21, no. 3, p. 035005, 2012.

[56] M. Pozzi and M. Zhu, “Plucked piezoelectric bimorphs for energy harvesting applications,” in *Smart Sensors, Actuators, and MEMS V*, vol. 8066, p. 806616, International Society for Optics and Photonics, 2011.

[57] S. Moss, A. Barry, I. Powlesland, S. Galea, and G. P. Carman, “A low profile vibro-impacting energy harvester with symmetrical stops,” *Applied Physics Letters*, vol. 97, no. 23, p. 234101, 2010.

[58] M. A. Halim, H. Cho, and J. Y. Park, “Design and experiment of a human-limb driven, frequency up-converted electromagnetic energy harvester,” *Energy Conversion and Management*, vol. 106, pp. 393–404, 2015.

[59] H. Fu and E. M. Yeatman, “A methodology for low-speed broadband rotational energy harvesting using piezoelectric transduction and frequency up-conversion,” *Energy*, vol. 125, pp. 152–161, 2017.

[60] S.-M. Jung and K.-S. Yun, “Energy-harvesting device with mechanical frequency-up conversion mechanism for increased power efficiency and wideband operation,” *Applied Physics Letters*, vol. 96, no. 11, p. 111906, 2010.

[61] H. Kulah and K. Najafi, “Energy scavenging from low-frequency vibrations by using frequency up-conversion for wireless sensor applications,” *IEEE Sensors Journal*, vol. 8, no. 3, pp. 261–268, 2008.

[62] A. S. Almansouri, K. N. Salama, and J. Kosel, “Magneto-acoustic resonator for aquatic animal tracking,” *IEEE Transactions on Magnetics*, vol. 55, no. 2, pp. 1–4, 2018.

[63] B. Marinkovic and H. Koser, “Smart sand—a wide bandwidth vibration energy harvesting platform,” *Applied Physics Letters*, vol. 94, no. 10, p. 103505, 2009.

[64] L. G. W. Tvedt, D. S. Nguyen, and E. Halvorsen, “Nonlinear behavior of an electrostatic energy harvester under wide-and narrowband excitation,” *Microelectromechanical Systems, Journal of*, vol. 19, no. 2, pp. 305–316, 2010.

[65] D. Miki, M. Honzumi, Y. Suzuki, and N. Kasagi, “Large-amplitude mems electret generator with nonlinear spring,” in *Micro Electro Mechanical Systems (MEMS), 2010 IEEE 23rd International Conference on*, pp. 176–179, IEEE, 2010.

[66] A. Erturk, J. Hoffmann, and D. Inman, “A piezomagnetoelastic structure for broadband vibration energy harvesting,” *Applied Physics Letters*, vol. 94, no. 25, p. 254102, 2009.

[67] A. Cammarano, S. Burrow, and D. Barton, “Modelling and experimental characterization of an energy harvester with bi-stable compliance characteristics,” *Proceedings of the Institution of Mechanical Engineers, Part I: Journal of Systems and Control Engineering*, vol. 225, no. 4, pp. 475–484, 2011.

[68] B. Ando, S. Baglio, C. Trigona, N. Dumas, L. Latorre, and P. Nouet, "Nonlinear mechanism in mems devices for energy harvesting applications," *Journal of Micromechanics and Microengineering*, vol. 20, no. 12, p. 125020, 2010.

[69] M. Ferrari, M. Bau, M. Guizzetti, and V. Ferrari, "A single-magnet nonlinear piezoelectric converter for enhanced energy harvesting from random vibrations," *Sensors and Actuators A: Physical*, vol. 172, no. 1, pp. 287–292, 2011.

[70] M. Ferrari, V. Ferrari, M. Guizzetti, B. Andò, S. Baglio, and C. Trigona, "Improved energy harvesting from wideband vibrations by nonlinear piezoelectric converters," *Sensors and Actuators A: Physical*, vol. 162, no. 2, pp. 425–431, 2010.

[71] J.-T. Lin, B. Lee, and B. Alphenaar, "The magnetic coupling of a piezoelectric cantilever for enhanced energy harvesting efficiency," *Smart materials and Structures*, vol. 19, no. 4, p. 045012, 2010.

[72] W. Al-Ashtari, M. Hunstig, T. Hemsel, and W. Sextro, "Frequency tuning of piezoelectric energy harvesters by magnetic force," *Smart Materials and Structures*, vol. 21, no. 3, p. 035019, 2012.

[73] L. Tang, H. Wu, Y. Yang, and C. K. Soh, "Optimal performance of nonlinear energy harvesters," in *22nd International Conference on Adaptive Structures and Technologies (ICAST)*, 2011.

[74] L. Tang, Y. Yang, and C.-K. Soh, “Improving functionality of vibration energy harvesters using magnets,” *Journal of Intelligent Material Systems and Structures*, vol. 23, no. 13, pp. 1433–1449, 2012.

[75] X. Li, Z. Li, H. Huang, Z. Wu, Z. Huang, H. Mao, and Y. Cao, “Broadband spring-connected bi-stable piezoelectric vibration energy harvester with variable potential barrier,” *Results in Physics*, vol. 18, p. 103173, 2020.

[76] R. M. Meneghini, M. M. Ziemba-Davis, L. R. Lovro, P. H. Ireland, and B. M. Damer, “Can intraoperative sensors determine the “target” ligament balance? early outcomes in total knee arthroplasty,” *The Journal of arthroplasty*, vol. 31, no. 10, pp. 2181–2187, 2016.

[77] K. A. Gustke, G. J. Golladay, M. W. Roche, L. C. Elson, and C. R. Anderson, “A new method for defining balance: promising short-term clinical outcomes of sensor-guided tka,” *The Journal of arthroplasty*, vol. 29, no. 5, pp. 955–960, 2014.

[78] M. Roche, L. Elson, and C. Anderson, “Dynamic soft tissue balancing in total knee arthroplasty,” *Orthopedic Clinics*, vol. 45, no. 2, pp. 157–165, 2014.

[79] S. Almouahed, C. Hamitouche, E. Stindel, and C. Roux, “Optimization of an instrumented knee implant prototype according to in-vivo use requirements,” in *Point-of-Care Healthcare Technologies (PHT), 2013 IEEE*, pp. 5–8, IEEE, 2013.

[80] S. R. Platt, S. Farritor, K. Garvin, and H. Haider, “The use of piezoelectric ceramics for electric power generation within orthopedic implants,” *IEEE/ASME transactions on mechatronics*, vol. 10, no. 4, pp. 455–461, 2005.

[81] S. R. Platt, S. Farritor, and H. Haider, “On low-frequency electric power generation with pzt ceramics,” *IEEE/ASME transactions on Mechatronics*, vol. 10, no. 2, pp. 240–252, 2005.

[82] B. E. Wilson, M. Meneghini, and S. R. Anton, “Embedded piezoelectrics for sensing and energy harvesting in total knee replacement units,” in *Active and Passive Smart Structures and Integrated Systems 2015*, vol. 9431, p. 94311E, International Society for Optics and Photonics, 2015.

[83] X. Cheng, X. Xue, Y. Ma, M. Han, W. Zhang, Z. Xu, H. Zhang, and H. Zhang, “Implantable and self-powered blood pressure monitoring based on a piezoelectric thinfilm: Simulated, in vitro and in vivo studies,” *Nano Energy*, vol. 22, pp. 453–460, 2016.

[84] Z. Pi, J. Zhang, C. Wen, Z.-b. Zhang, and D. Wu, “Flexible piezoelectric nanogenerator made of poly (vinylidenefluoride-co-trifluoroethylene)(pvdf-trfe) thin film,” *Nano Energy*, vol. 7, pp. 33–41, 2014.

[85] K.-I. Park, M. Lee, Y. Liu, S. Moon, G.-T. Hwang, G. Zhu, J. E. Kim, S. O. Kim, D. K. Kim, Z. L. Wang, *et al.*, "Flexible nanocomposite generator made of batio3 nanoparticles and graphitic carbons," *Advanced Materials*, vol. 24, no. 22, pp. 2999–3004, 2012.

[86] G.-T. Hwang, H. Park, J.-H. Lee, S. Oh, K.-I. Park, M. Byun, H. Park, G. Ahn, C. K. Jeong, K. No, *et al.*, "Self-powered cardiac pacemaker enabled by flexible single crystalline pmn-pt piezoelectric energy harvester," *Advanced materials*, vol. 26, no. 28, pp. 4880–4887, 2014.

[87] Y. Zi, J. Wang, S. Wang, S. Li, Z. Wen, H. Guo, and Z. L. Wang, "Effective energy storage from a triboelectric nanogenerator," *Nature communications*, vol. 7, 2016.

[88] Z. L. Wang, "Triboelectric nanogenerators as new energy technology and self-powered sensors–principles, problems and perspectives," *Faraday discussions*, vol. 176, pp. 447–458, 2015.

[89] F.-R. Fan, Z.-Q. Tian, and Z. L. Wang, "Flexible triboelectric generator," *Nano Energy*, vol. 1, no. 2, pp. 328–334, 2012.

[90] Z. L. Wang, "Triboelectric nanogenerators as new energy technology for self-powered systems and as active mechanical and chemical sensors," *ACS nano*, vol. 7, no. 11, pp. 9533–9557, 2013.

[91] A. Ibrahim, M. Jain, E. Salman, R. Willing, and S. Towfighian, "Feasibility of triboelectric energy harvesting and load sensing in total knee replacement," in *ASME 2018 Conference on Smart Materials, Adaptive Structures and Intelligent Systems*, pp. V002T07A016–V002T07A016, American Society of Mechanical Engineers, 2018.

[92] A. Ibrahim, G. Yamomo, R. Willing, and S. Towfighian, "Analysis of a triboelectric energy harvester for total knee replacements under gait loading," in *Active and Passive Smart Structures and Integrated Systems XIII*, vol. 10967, p. 109671D, International Society for Optics and Photonics, 2019.

[93] E. H. Ledet, B. Liddle, K. Kradinova, and S. Harper, "Smart implants in orthopedic surgery, improving patient outcomes: a review," *Innovation and entrepreneurship in health*, vol. 5, p. 41, 2018.

[94] M. Sloan, A. Premkumar, and N. P. Sheth, "Projected volume of primary total joint arthroplasty in the us, 2014 to 2030," *JBJS*, vol. 100, no. 17, pp. 1455–1460, 2018.

[95] R. E. Anakwe, P. J. Jenkins, and M. Moran, "Predicting dissatisfaction after total hip arthroplasty: a study of 850 patients," *The Journal of arthroplasty*, vol. 26, no. 2, pp. 209–213, 2011.

[96] M. S. Kuster, "Exercise recommendations after total joint replacement," *Sports medicine*, vol. 32, no. 7, pp. 433–445, 2002.

[97] G. Bergmann, F. Graichen, and A. Rohlmann, “Hip joint contact forces during stumbling,” *Langenbeck’s Archives of Surgery*, vol. 389, no. 1, pp. 53–59, 2004.

[98] U. Marschner, H. Grätz, B. Jettkant, D. Ruwisch, G. Woldt, W.-J. Fischer, and B. Clasbrummel, “Integration of a wireless lock-in measurement of hip prosthesis vibrations for loosening detection,” *Sensors and Actuators A: Physical*, vol. 156, no. 1, pp. 145–154, 2009.

[99] W. Hodge, K. Carlson, R. Fijan, R. Burgess, P. Riley, W. Harris, and R. Mann, “Contact pressures from an instrumented hip endoprosthesis.,” *JBJS*, vol. 71, no. 9, pp. 1378–1386, 1989.

[100] G. Bergmann, F. Graichen, A. Rohlmann, A. Bender, B. Heinlein, G. Duda, M. Heller, and M. Morlock, “Realistic loads for testing hip implants,” *Bio-medical materials and engineering*, vol. 20, no. 2, pp. 65–75, 2010.

[101] F. Burny, M. Donkerwolcke, F. Moulart, R. Bourgois, R. Puers, K. Van Schuylenbergh, M. Barbosa, O. Paiva, F. Rodes, J. B. Bégueret, *et al.*, “Concept, design and fabrication of smart orthopedic implants,” *Medical engineering & physics*, vol. 22, no. 7, pp. 469–479, 2000.

[102] J. Andreu-Perez, D. R. Leff, H. M. Ip, and G.-Z. Yang, “From wearable sensors to smart implants—toward pervasive and personalized healthcare,” *IEEE Transactions on Biomedical Engineering*, vol. 62, no. 12, pp. 2750–2762, 2015.

[103] C. O’Connor and A. Kiourti, “Wireless sensors for smart orthopedic implants,” *Journal of Bio-and Tribo-Corrosion*, vol. 3, no. 2, p. 20, 2017.

[104] P. Sell, “Instrumented implants in orthopaedics,” *Journal of biomedical engineering*, vol. 11, no. 2, pp. 111–112, 1989.

[105] E. H. Ledet, D. D’Lima, P. Westerhoff, J. A. Szivek, R. A. Wachs, and G. Bergmann, “Implantable sensor technology: from research to clinical practice,” *JAAOS-Journal of the American Academy of Orthopaedic Surgeons*, vol. 20, no. 6, pp. 383–392, 2012.

[106] M. Younis, *MEMS Linear and Nonlinear Statics and Dynamics.* Microsystems, Springer US, 2011.

[107] K. R. Kaufman, N. Kovacevic, S. E. Irby, and C. W. Colwell, “Instrumented implant for measuring tibiofemoral forces,” *Journal of biomechanics*, vol. 29, no. 5, pp. 667–671, 1996.

[108] I. Kutzner, B. Heinlein, F. Graichen, A. Bender, A. Rohlmann, A. Halder, A. Beier, and G. Bergmann, “Loading of the knee joint during activities of daily living measured in vivo in five subjects,” *Journal of biomechanics*, vol. 43, no. 11, pp. 2164–2173, 2010.

[109] A. Diaz and R. Felix-Navarro, “A semi-quantitative tribo-electric series for polymeric materials: the influence of chemical structure and properties,” *Journal of Electrostatics*, vol. 62, no. 4, pp. 277–290, 2004.

[110] L. Dhakar, P. Pitchappa, F. E. H. Tay, and C. Lee, “An intelligent skin based self-powered finger motion sensor integrated with triboelectric nanogenerator,” *Nano Energy*, vol. 19, pp. 532–540, 2016.

[111] U. Khan, T.-H. Kim, H. Ryu, W. Seung, and S.-W. Kim, “Graphene tribotronics for electronic skin and touch screen applications,” *Advanced materials*, vol. 29, no. 1, p. 1603544, 2017.

[112] A. Ibrahim, M. Jain, E. Salman, R. Willing, and S. Towfighian, “A smart knee implant using triboelectric energy harvesters,” *Smart Materials and Structures*, vol. 28, no. 2, p. 025040, 2019.

[113] M. Jain, A. Ibrahim, E. Salman, M. Stanacevic, R. Willing, and S. Towfighian, “Frontend electronic system for triboelectric harvester in a smart knee implant,”

in *2019 IEEE 62nd International Midwest Symposium on Circuits and Systems (MWSCAS)*, pp. 386–389, IEEE, 2019.

[114] J. Henniker, "Triboelectricity in polymers," 1962.

Appendices

Appendix A: Coefficients of Magnetic Force

$$
\begin{aligned}
\alpha_1 &= \frac{F_R(d^2 - 4Y_s^2)}{(d^2 + Y_s^2)^{7/2}} \\
\alpha_2 &= \frac{5F_R Y_s(-3d^2 + 4Y_s^2)}{2(d^2 + Y_s^2)^{9/2}} \\
\alpha_3 &= \frac{5F_R(d^4 - 12d^2Y_s^2 + 8Y_s^4)}{2(d^2 + Y_s^2)^{11/2}} \\
\alpha_4 &= \frac{35F_R Y_s(5d^4 - 20d^2Y_s^2 + 8Y_s^4)}{8(d^2 + Y_s^2)^{13/2}} \\
\alpha_5 &= \frac{7F_R(5d^6 - 120d^4Y_s^2 + 240d^2Y_s^4 - 64Y_s^6)}{8(d^2 + Y_s^2)^{15/2}} \\
\alpha_6 &= \frac{21F_R Y_S(-35d^6 + 280d^4Y_s^2 - 336d^2Y_s^4 + 64Y_s^6)}{16(d^2 + Y_s^2)^{17/2}} \\
\alpha_7 &= \frac{15F_R(7d^8 - 280d^6Y_s^2 + 1120d^4Y_s^4 - 896d^2Y_s^6 + 128Y_s^8)}{16(d^2 + Y_s^2)^{19/2}} \\
\alpha_8 &= \frac{165F_R Y_s(63d^8 - 840d^6Y_s^2 + 2016d^4Y_s^4 - 1152d^2Y_s^6 + 128Y_s^8)}{128(d^2 + Y_s^2)^{21/2}} \\
\alpha_9 &= \frac{55F_R(-21d^{10} + 1260d^8Y_s^2 - 8400d^6Y_s^4 + 13440d^4Y_s^6 - 5760d^2Y_s^8 + 512Y_s^{10})}{128(d^2 + Y_s^2)^{23/2}}
\end{aligned}
\tag{1}
$$